Reconciling fast and slow cooling during planetary formation as recorded in the main group pallasites

M. Murphy Quinlan*[1] A. M. Walker[2] C. J. Davies[1]

*Email: eememq@leeds.ac.uk
[1] *School of Earth and Environment, University of Leeds, Leeds, UK*
[2] *Department of Earth Sciences, University of Oxford, Oxford, UK*

May 8, 2023

Both the main text of the manuscript an the supplementary information are included in this document.

The source code used for the numerical modelling in this study can be found at `https://github.com/murphyqm/pytesimint` and `https://github.com/murphyqm/pytesimal`.

Reconciling fast and slow cooling during planetary formation as recorded in the main group pallasites

M. Murphy Quinlan*[1]   A. M. Walker[2]   C. J. Davies[1]

*Email: eememq@leeds.ac.uk
[1]*School of Earth and Environment, University of Leeds, Leeds, UK*
[2]*Department of Earth Sciences, University of Oxford, Oxford, UK*

May 8, 2023

Abstract

Pallasite meteorites contain evidence for vastly different cooling timescales: rapid cooling at high temperatures (K/years) and slow cooling at lower temperatures (K/Myrs). Pallasite olivine also shows contrasting textures ranging from well-rounded to angular and fragmental, and some samples record chemical zoning. Previous pallasite formation models have required fortuitous changes to the parent body in order to explain these contrasting timescales and textures, including late addition of a megaregolith layer, impact excavation, or parent body break-up and recombination. We investigate the timescales recorded in Main Group Pallasite meteorites with a coupled multiscale thermal diffusion modelling approach, using a 1D model of the parent body and a 3D model of the metal-olivine intrusion region, to see if these large-scale changes to the parent body are necessary. We test a range of intrusion volumes and aspect ratios, metal-to-olivine ratios, and initial temperatures for both the background mantle and the intruded metal. We find that the contrasting timescales, textural heterogeneity, and preservation of chemical zoning can all occur within one simple ellipsoidal segment of an intrusion complex. These conditions are satisfied in 13 % of our randomly generated models (2200 model runs), with small intrusion volumes (with a mean radius $\lesssim$ 100 m) and colder background mantle temperatures ($\lesssim$ 1200 K) favourable. Large rounded olivine can be explained by a previous intrusion of metal into a hotter mantle, suggesting possible repeated bombardment of the parent body. We speculate that the formation of pallasitic zones within planetesimals may have been a common occurence in the early Solar System, as our model shows that favourable pallasite conditions can be accommodated in a wide range of intrusion morphologies, across a wide range of planetesimal mantle temperatures, without the need for large-scale changes to the parent body. We suggest that pallasites represent a late stage of repeated injection of metal into a cooling planetesimal mantle, and that heterogneity observed in micro-scale rounding or chemical zoning preservation in pallasite olivine can be explained by diverse cooling rates in different regions of a small intrusion.

1 Introduction

Main Group Pallasite meteorites (referred to from here on as “pallasites”), consisting of a mixture of silicate crystals (predominantly forsteritic olivine) and FeNi alloy, are believed to represent a key time in the early evolution of the solar system as metal differentiated from silicate and planetary cores began to form. However, models differ about the exact details of the process represented by the pallasite meteorites. In particular, pallasites contain evidence for cooling at contrasting timescales: the metal portion records cooling at rates of $\sim 10^{-6}$–10^{-5} Kelvin per year below $\sim$ 900 K (Ni diffusion studies; Yang et al., 1997, 2010; Goldstein et al., 2014), while orders of magnitude more rapid cooling ($\sim 10^{0}$–10^{2} Kelvin per year) has been suggested to explain chemical gradients and heterogeneity in olivine acquired at higher temperatures (Miyamoto, 1997; Tomiyama and Huss, 2006), and the halted textural equilibration post-metal-injection (Walte and Golabek, 2022). The difference between these rates cannot be explained by a simple conductive cooling model of a planetesimal that initially cools rapidly and then slows (Yang et al., 2010).

The macro-scale texture of pallasite olivine across and within samples ranges from well-rounded to fragmental and highly angular (Grossman and Nomenclature Committee of the Meteoritical Society, 2022). While not systematically addressed in the literature, the degree of micro-scale rounding also appears to vary across samples, with macroscopically angular olivine grains frequently having microscopically rounded corners (Scott, 1977). The degree of rounding of olivine grains increases with residence time in hot FeNi (Saiki et al., 2003; Walte et al., 2020), and so the range in degree of olivine angularity across pallasite samples adds further constraints on the cooling rate of the intruded metal in contact with said olivine. The heterogeneity of olivine textures may indicate different formation environments for rounded versus angular olivine crystals, with different temperatures, cooling rates and residence times in molten FeNi metal (McKibbin et al., 2019).

Previous models have suggested injection of metal into a planetesimal mantle via a metallic bolide (Tarduno et al., 2012) or ferrovolcanism from the planet's molten core (Johnson et al., 2020) in order to explain the delivery of molten metal into the parent body mantle. Metal intrusion formation models typically include a qualitative description of large-scale changes to the parent body following metal intrusion to explain the contrasting timescales recorded in pallasite samples, including impact-related excavation to enable rapid cooling of olivine, the late addition of a thick megaregolith blanket to slow cooling at lower temperatures after the olivine cooling rates were recorded, or the break-up and/or re-combination of the parent body (Bryson et al., 2015; Walte et al., 2020; Yang et al., 2010). Walte et al. (2020) suggest the presence of a small fraction (2–15 vol. %) of 'primary' metal trapped in the parent body mantle before the intrusion of 'secondary' metal from a bolide, either as residual metal from incomplete parent-body differentiation, or delivered by an earlier impact and subsequently texturally equilibrated (Walte and Golabek, 2022), to facilitate rounding and grain-growth of the largest fraction of rounded olivines over geological timescales, and to aid later migration of metal melt through the mantle (Saiki et al., 2003).

The observed cooling-rate constraints and textural details have previously been studied in isolation or included in descriptive formation hypotheses, and have not been integrated into a single quantitative model to address whether large-scale changes to the parent body or different formation environments are required to produce the diversity of time scales and textures seen across Main Group Pallasites.

We model the rapid thermal evolution of a metal-olivine intrusion within a slowly cooling mantle in order to test whether we can reproduce the recorded cooling rates and observed olivine textures in pallasite samples without ad-hoc changes to the parent body. We assume a separation of timescales such that there is a one-way interaction between slow cooling of the planetesimal and the fast evolution of the intrusion: the planetesimal mantle temperature sets the initial and boundary conditions of the metallic intrusion, but this small metallic intrusion does not influence the slow, large-scale cooling of the planetesimal mantle. We also investigate the effect of the inclusion of a small fraction of metal in the planetesimal mantle, both on the cooling of the parent body, and on the cooling of later intrusions into the mantle, in order to address the possibility of a multi-collisional formation with earlier stranded metal in the mantle. We discuss the existence of other meteorite groups under the umbrella textural term "pallasite" that formed in different parent bodies, in distinct regions of the Solar System, and what this implies for the planetary building process.

2 Numerical model of a metal intrusion

Our conceptual approach of coupling the large-scale, long-term cooling of the pallasite parent body, to the small-scale, rapid cooling of the intrusion region, can be summarised in five steps (labelled with corresponding numbers in Figure 1):

Step 1. We model the 1D temperature evolution of a simple three-layered parent body, using the method and planetesimal geometry of the best-fitting result of Murphy Quinlan et al. (2021a): a thick-mantled 250 km radius planetesimal with a core radius of 125 km, and an 8 km-thick megaregolith layer that does not vary in thickness with time. We repeat this body geometry, with the addition of 15 vol. % metal in the mantle, as an upper end-member (based on the upper limit of primary metal fraction found in Seymchan, Walte et al. 2020). We also use an example result from Nichols et al. (2021): a thin-mantled

300 km radius body with a 250 km radius core, and an 8 km-thick blanket of megaregolith that does not vary in thickness with time.

Step 2. We use the output of step 1 (a time series of temperatures and cooling rates along radius) to calculate a residence depth for the Imilac meteorite in each parent body, based on the metallographic cooling rates recorded by Ni diffusion between kamacite and taenite (Yang et al., 2010; Bryson et al., 2015). We infer that this cooling rate is recorded after metal injection, once the metal has cooled to the background mantle temperature of the parent body, and that it captures the large-scale cooling of the planetesimal mantle. We focus on this one meteorite as an example, but our results are general and can be applied across the suite of pallasite meteorites.

Step 3. We extract temperature profiles along the planetesimal's radius, centered at the residence depth calculated in step two, at times earlier than the metal cooling rates were recorded. We interpolate these temperature profiles so that they can be used at a smaller metre-scale grid size.

Step 4. We consider a cube of mantle material with a vertical temperature gradient set by the background mantle 1D temperature profile from step three.

Step 5. We place an ellipsoid with the material properties of mixed metal and forsteritic olivine in the centre of this cartesian box, with an elevated temperature relative to the background mantle (above the liquidus of FeNi metal, but below the solidus of the forsterite), and allow it to cool and crystallise while determining the region's 3D temperature field. Our use of 3-dimensional geometry (as opposed to 1- or 2D) allows us to represent a finite ellipsoid encapsulated by mantle with an asymmetric initial temperature condition along z.

Steps 4 and 5 are developed and discussed in more detail below; information regarding the earlier steps can be found in Murphy Quinlan et al. (2021a). We use the Imilac meteorite due to paleomagnetic measurements that add an additional constraint regarding core crystallisation timing (Bryson et al., 2015), but our model set-up and assumptions can also be applied to other Main Group Pallasite samples. An inherent assumption of our model is that there is a separation of timescales, implying that there is only one-way interaction between the slowly cooling parent body mantle, and the rapidly cooling intrusion: while the mantle temperature sets the boundary condition and initial temperature field of the intrusion model, the intrusion does not affect the large scale cooling of the mantle. We assume instantaneous emplacement of the molten metal and do not model deformation associated with intrusion. The results of this intrusion model are then compared to the evidence from pallasite samples for preservation of chemical heterogeneity and rounding of olivines to see whether the conditions are favourable for reproducing the known pallasite samples in the meteorite record.

2.1 Modelling the intrusion region

Our intrusion model consists of an ellipsoidal region of interconnected solid olivine bridgework (Boesenberg et al., 2012), the pore space (created by impact-related inter- and intra-granular fracturing) of which has been infiltrated and saturated by initially molten FeNi metal. This intrusion region is centered in a box of mantle material (Figure 1; steps 4 and 5) that is below the FeNi solidus. We assume convection of the metal in this region is inhibited by the low porosity and permeability of the solid olivine bridgework, the crystallisation of the metal, and the low gravitational acceleration.

We consider a cartesian box of mantle material with constant temperature in the horizontal directions x and y, and the vertical coordinate z aligned with the 1D mantle temperature output from the planetesimal model (Figure 1; part three). Assuming a purely conductive system in which convective heat transport and internal heat generation are neglected, the temperature T (K) in this volume satisfies the three-dimensional heat conduction equation (Carslaw and Jaeger, 1959):

$$\rho c_p \frac{\partial T}{\partial t} = \frac{\partial}{\partial x}\left(k\frac{\partial T}{\partial x}\right) + \frac{\partial}{\partial y}\left(k\frac{\partial T}{\partial y}\right) + \frac{\partial}{\partial z}\left(k\frac{\partial T}{\partial z}\right) \tag{1}$$

where: ρ is the density of the material ($\mathrm{kg\,m^{-3}}$); c_p is the specific heat capacity ($\mathrm{J\,kg^{-1}\,K^{-1}}$); t is time (s); x, y, and z are the spatial coordinates (m); and k is thermal conductivity ($\mathrm{W\,m^{-1}\,K^{-1}}$). We choose

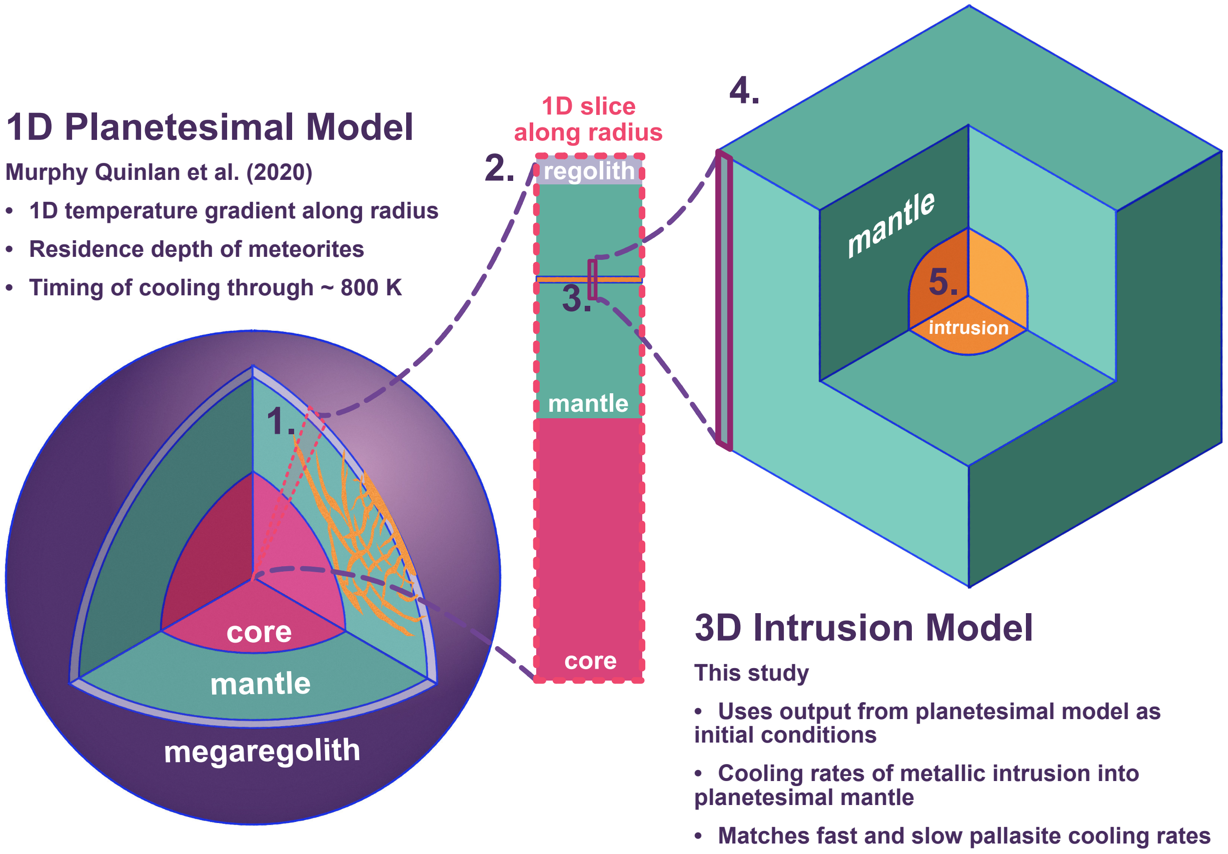

Figure 1: Cartoon sketch of model set up; not to scale. 1D temperature, cooling rate, and pallasite residence depth estimation output from the planetesimal model of Murphy Quinlan et al. (2021a) are used as input for a 3D intrusion model; the numbers refer to the modelling method steps laid out in section 2.

temperature-independent k, allowing the Crank-Nicolson scheme to be applied to the problem without the complications associated with non-linearity (Carslaw and Jaeger, 1959; Özısık, 1993).

We define a uniaxial ellipsoid of volume $V = \frac{4}{3}\pi a^2 b$, where a and b are radii, which represents the intrusion region with a pallasitic mix of silicate and metal. The dimensions of the box ($X = Y = Z$), within which this ellipsoid is centered, is set by the diffusion lengthscale for the mantle material: we wish to run the model for ten years, and do not want the temperature near the model boundaries to change during that time. This allows us to apply a zero-flux condition to the boundaries of the problem.

Directly modelling the mixed-phase region of olivine crystals and metal melt would be computationally expensive and require detailed knowledge of the geometry of the phase mixture, which we do not know. Instead, we take a macroscopic approach to track the cooling and crystallisation of the metal in this area, and consider the intrusion region as a single material, using volume-averaged effective thermal properties. We adopt the method of Mottaghy and Rath (2006) to model permafrost: we assume a simple saturated two component system, where olivine forms a solid interconnected bridgework of crystals, with the pore space filled with metal.

The fraction of solid and liquid metal is controlled by a temperature-dependent function which should be one when the metal is entirely solid ($T < T_S$, the FeNi solidus temperature), and zero when the metal is fluid ($T > T_L$, the FeNi liquidus temperature). In order to account for the latent heat associated with melting or crystallisation, we apply the simple fixed-domain apparent heat capacity method (Figure S1 in the supplementary material) which correlates the heat capacity of the phase-changing material with the slope of the enthalpy-temperature curve (Zeneli et al., 2021, further details in supplementary materials).

The material properties outside the intrusion region have constant values that match that of olivine, or a mixture of olivine and 15 vol. % metal; however, phase change processes are not considered for the metal in this region. Sudden jumps and step functions in the spatially-varying diffusivity can introduce instabilities especially if these material properties boundaries intersect with the model boundary, so we surround our intrusion region with mantle material and ensure spatially-constant material properties at the model boundaries.

We apply the semi-implicit Crank-Nicolson scheme (Crank and Nicolson, 1947) due to its stability with zero-flux boundary conditions to the heat equation in 1D. Forward difference is used for the time derivative of T, but the spatial derivative is evaluated at the time step $t + \Delta t/2$ instead of at t, taking the arithmetic mean between the time step t and $t + \Delta t$. We also discretise κ with respect to distance using finite differences (Langtangen and Linge, 2017). In order to extend this scheme to three dimensions, we apply the Fractional Step Method (Cen et al., 2016; Yanenko, 1971), which evaluates the heat equation in one-third time step increments along each of the spatial dimensions.

We bench-marked our numerical model against an analytical solution from Carslaw and Jaeger (1959), and found that the maximum relative defect between the numerical and analytical models dropped to below 1 % within 150 seconds (Figure S2). We also investigated the effect of spatial and temporal resolution on our results to ensure we chose a sufficiently small step size (Figure S3). Extended methods and full derivations can be found in the supplementary information.

3 Quantitative constraints on the cooling of pallasite meteorites

The results of the model at different times are analysed and compared to the meteorite record. We address two key criteria: the potential for rounding of olivine grains, and the preservation of primary igneous zoning. Each intrusion model output is scored based on whether it was consistent with observations from the meteorite record with respect to these criteria; models with a score of two reproduce both results.

3.1 Textural heterogeneity

While the macro-scale textural heterogeneity of pallasite olivines is a striking feature that has previously been used to attempt to constrain formation mechanisms (for instance, McKibbin et al., 2019), pallasite samples also display textural heterogeneity on the micro-scale. Scott (1977) recorded the presence of apparently spheroidal sub-millimetre olivine grains alongside macroscopically angular olivine, and noted that while the degree of microscopic rounding of olivine grains varied across samples, when magnified, many angular olivine grains have rounded corners. This is supported also by Buseck (1977), who stated that 'almost all' sharp olivine corners appear to have been somewhat microscopically rounded following fragmentation.

Small olivine grains of diameter 300 μm, or the corners of larger olivine fragments, could be rounded within approximately ten years in Fe-Ni-S at temperatures at or above $\sim$ 1573 K, or within approximately three months at $\sim$ 1623 K (Walte et al., 2020; Saiki et al., 2003). Larger olivines could also be rounded on geologically short timescales at higher temperatures, or with protracted cooling, or in the presence of sulfide-rich metal melt (Solferino et al., 2015).

Based on experimental results from Walte et al. (2020), to round small olivine grains we require a point within the intrusion region to be at or above 1623 K at three months after the start of the model run, or at or above 1573 K at ten years after the start of the model run. We investigate the sensitivity of the model to these requirements by both varying the temperature cut-offs by ±10% and by varying the timing of the measurement, and find that the earliest requirement ($T \geq 1623$ K at three months) is the most sensitive both to changing the time or temperature of this requirement (see Figure S4). As the temperature constraints are derived from two preliminary experimental results recorded at the temperatures listed extrapolated multiple orders of magnitude beyond the original experimental design (i.e. from hours and seconds to months and years), and the texture estimates are based on arbitrary estimates of the gross statistical properties of the incomplete meteorite record, incorporating an estimate of error on the constraints would imply an unrealistic level of precision.

As micro-scale rounding of olivine in pallasite meteorites has not been systematically surveyed, we vary the volume requirement of the intrusion that must cool slowly enough to meet the above criteria between $\geq$ 30 % and $\geq$ 70 % by volume. For the main suite of results presented in this paper, we require that $\geq$ 40 % by volume of the intrusion region cools slowly enough to enable micro-scale rounding. This arbitrary lower limit takes into account the isothermal nature of the experiments presented by Walte et al. (2020). As our starting temperature is higher than the experimental temperatures that were held constant while investigating rounding (1623 K and 1573 K), a shorter time at elevated temperatures will actually be required, leading our model to underestimate the rounded fraction of the intrusion.

Scott (2017) suggested that the macro-morphology of rounded-type pallasites (for example, Brenham, with cm-scale spheroidal olivine grains) predates the fragmentation of olivine clusters and intrusion of the main bulk of pallasite metal (the intrusion modelled in this study). These large, well rounded grains may have formed in contact with sizeable metal pockets that were trapped in the planetesimal mantle either during core-mantle differentiation (Scott, 2017) or through repeated impact delivery of metal to the planetesimal (Walte et al., 2020; Walte and Golabek, 2022). This pre-fragmentation trapped metal is referred to as 'primary metal' hereafter, while the later metal intrusion is referred to as 'secondary metal'.

We address the possible retention of primary metal by increasing the average diffusivity of the parent body mantle for a selection of runs, to approximate a macroscopic mixture of metal and olivine, and track the cooling history at the depth of pallasite residence to see if large-scale rounding can be achieved prior to secondary metal intrusion. While we examine this early process further in the discussion, our modelling primarily focuses on the micro-scale rounding in secondary metal.

Macroscopically 'mixed-type' pallasites can potentially be explained by pieces of angular or rounded olivine being broken off the bridgework and entrained in the secondary metal melt, and carried to regions with olivine of a different morphology, followed by cooling which preserved the macroscopic textural heterogeneity; alternatively early sub-solidus convection of the parent-body mantle could redistribute and mix different olivine morphologies from different source regions in the mantle (Solferino and Golabek, 2018). Further study on the microscopic textures of pallasite olivine are required to determine the extent of heterogeneity within and between samples; mixing in the intrusion region and rapid cooling could similarly be invoked to explain any observed contrasts within single samples.

3.2 Chemical heterogeneity

Pallasite olivines display heterogeneous core and rim compositions (Hsu, 2003), with potential oscillatory zoning in Cr, Al and V recorded in the Imilac meteorite (Chernonozhkin et al., 2021). Preservation of original igneous compositions is varied, with solid-state diffusive modification of different elements on different scales recorded across samples (Hsu, 2003). In general, Ca zoning (either diffusion profiles or original heterogeneity) is pervasive in pallasite olivine and has not been completely homogenised (Hsu, 2003).

In an olivine grain of diameter 300–500 μm, Ca will be completely homogenised within four years at $\sim$ 1573 K and within 8 years at $\sim$ 1373 K (Hsu, 2003; Jurewicz and Watson, 1988). This means that to preserve the Ca heterogeneity in pallasite olivine, including in the smallest size fraction, the majority of pallasite samples had to cool rapidly enough to prevent this erasure.

Based on diffusion studies of Hsu (2003) and Jurewicz and Watson (1988), to preserve zoning we require that a point within the intrusion region cools below 1573 K within four years, and below 1373 K within eight years. In order to reproduce the "ubiquitous" preservation of Ca zoning observed in the pallasite meteorite record (Hsu, 2003), we require that ≥ 90 % by volume of the intrusion region cools rapidly enough to preserve Ca zoning. As with the rounding criteria, we also varied this requirement, down to a lower limit of ≥ 30 % by volume, to allow for variations in degree of diffusional modification, to test if this changes the overall trend of results. We use the lower cut-off value of ≥ 50 % for our example case (Fig. 2) to better illustrate our point-by-point filtering approach, but use the stricter ≥ 90 % cut-off when looking at the overall suite of models, and unless otherwise specified refer to this as the zoning requirement. As with the rounding criteria, we allowed the temperature requirements to vary by ±10%, and investigated the sensitivity of the model to the times these filters were applied (Figure S4).

3.3 Filtering model output

We analyse each model run's 3D temperature array at three months, four years, eight years, and ten years and find the volume of the intrusion region that meets each of the following logical criteria:

$$\begin{aligned} R &:= (T_{\text{3mnths}} \geq 1623\,\text{K}) \;\vee\; (T_{\text{10yrs}} \geq 1573\,\text{K}), \\ Z &:= (T_{\text{4yrs}} \quad \leq 1573\,\text{K}) \;\wedge\; (T_{\text{8yrs}} \;\; \leq 1373\,\text{K}), \end{aligned} \tag{2}$$

where R represents potential rounding, and Z denotes potential zoning. Based on the meteorite record (Grossman and Nomenclature Committee of the Meteoritical Society, 2022; see supplementary information) we assign a score to the model output:

- If $\geq x$ vol. % of the intrusion will round olivine crystals, and $\geq y$ vol. % will preserve Ca heterogeneity, the output receives a score of two. For the main body of this study, we require rounding in ≥ 40 vol. % and zoning in ≥ 90 vol. % of the intrusion region, but for our example model run (figures 2 and 3) we use a requirement of ≥ 50 vol. % for both rounding and zoning as it is more illustrative of our method. We additionally test a suite of different filter requirements, ranging from $\geq$ 30–90 vol. % (see supplementary information).
- If the intrusion region meets only one of these criteria, the output receives a score of one.
- If neither constraint is met, the output receives a null score.

We use this simple scoring criteria instead of alternative measures of goodness-of-fit as we are primarily interested in whether any models can match these criteria, as opposed to investigating in detail what region of parameter space best reproduces certain results. This can be addressed in future work, as the Euclidean norm or a similar measurement can be easily incorporated into our framework. We also test the sensitivity of the overall score to changing the rounding and zoning criteria. We find that for a spatial step $\Delta x < 4$ m or time step $\Delta t \leq 1$ month, the result is not impacted by the spatial or temporal resolution of the model (Figure S3).

4 Cooling of a metal intrusion

Using the best-fitting model of Murphy Quinlan et al. (2021a), we initially modelled the temperature evolution of the mantle of a 250 km radius planetesimal and calculated the residence depth of the Imilac pallasite meteorite based on Ni-diffusion cooling rates estimated from its metal portion (Figure 2a; Murphy Quinlan et al., 2021a; Yang et al., 2010; Bryson et al., 2015). The vertical temperature gradient through the mantle at an earlier time (selected at random, Figure 2b) was then used as the initial condition for the metal intrusion model (Figure 2c and d). The parameters used for this model are given in Table 1. Additional 3D temperature arrays plots in the supplementary information (Figures S5, S6).

Parameter	Symbol	Unit	Range/Value	Example model run	References/Notes
Initial/boundary conditions					
Intrusion radii	r_x, r_y, r_z	m	10–150	72, 72, 92	
Mean radius	$\overline{r}$	m	11–147	79	
Unique/non-unique axes	b/a		0.07–15.0	1.28	
Metal fraction (intrusion)	ϕ_m	vol. fraction	0.05–0.55	0.32	Met. Bull. Database
Trapped metal (in mantle)		vol. fraction	0–0.2	0	Walte et al. (2020)
Background mantle temp.—top	T_t	K	250–1600 (804–1600)	847	Murphy Quinlan et al. (2021a)
Background mantle temp.—bottom	T_b	K	260–1685 (808–1600)	851	Murphy Quinlan et al. (2021a)
Initial intrusion temp.	T_i	K	1600–1900	1660	Assumed to be above metal liquidus due to impact heating
Material properties					
Metal					
Density	ρ_m	kg m^{-3}	7020–7500	7260	Scheinberg et al. (2016)
Conductivity	k_m	W m^{-1} K^{-1}	30–40	35	Scheinberg et al. (2016); Touloukian et al. (1971)
Heat capacity	c_m	J kg^{-1} K^{-1}	820–850	835	Desai (1986)
Diffusivity	κ_m	m^2 s^{-1}	$k_m/(\rho_m c_m)$		
Latent heat of crystallisation	L	J kg^{-1}	1.33×10^5 – 2.7×10^5	2.56×10^5	Scheinberg et al 2016
Liquidus temperature	T_L	K	1570–1810	1600	Ehlers (1972)
Solidus temperature	T_S	K	1260–1790	1260	Ehlers (1972)
Olivine					
Density	ρ_{ol}	kg m^{-3}	3320–3360	3341	Su et al. (2018)
Conductivity	k_{ol}	W m^{-1} K^{-1}	2.5–3.4	3	Murphy Quinlan et al. (2021a); Bryson et al. (2015)
Heat capacity	c_{ol}	J kg^{-1} K^{-1}	810–830	819	Su et al. (2018)
Diffusivity	κ_{ol}	m^2 s^{-1}	$k_{ol}/(\rho_{ol} c_{ol})$		
Numerical details					
Time step	Δt	s	2.63×10^6	2.63×10^6	Approx. 1 month
Spatial step	Δx, Δy, Δz	m	2	2	Calculated from L, N
Box size	L_x, L_y, L_z	m	200–800	400	
Number of nodes	N_x, N_y, N_z		101– 401	201	L and N balanced to give $\Delta x, y, z = 2$ m
Total iterations			10– 241	121	
Boundary conditions	$\mathbf{b}^n$, $\mathbf{b}^{n+1}$		Neumann, Dirichlet	Zero flux (Neumann)	
Outputs					
Actual intrusion volume	V	m^3	4.90×10^3–1.38×10^7	1.998×10^6	
Percentage zoning preserved	Z %	%	0 – 100	67.2	
Percentage rounded	R %	%	0 – 100	66.7	

Table 1: Ranges of parameter values for 2200 model runs, including example model run illustrated in Figures 2 and 3. Mantle background temperatures show the range for randomised runs, with planetesimal-model informed ranges in round brackets. Ranges given do not include parameter variation for sensitivity testing and benchmarking (see supplementary material for further information).

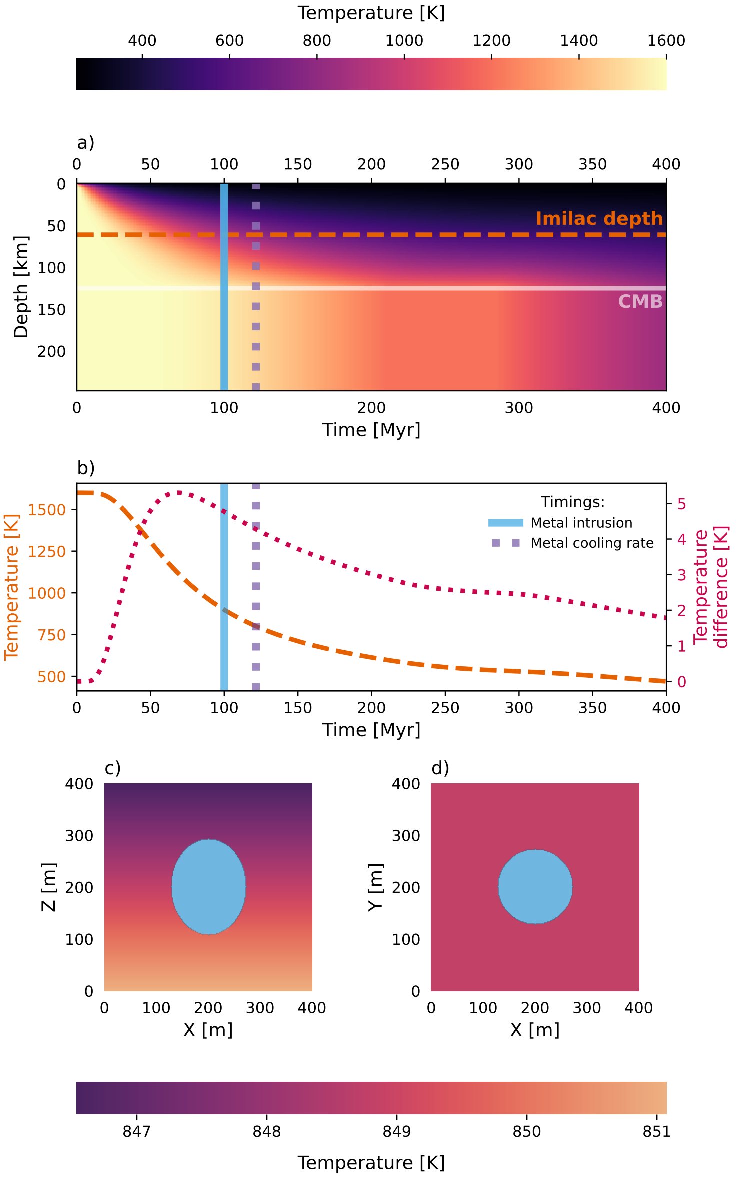

Figure 2: Initial conditions for model run. (a) The 1D temperature evolution for a 250 km radius planetesimal with a 125 km radius core and an 8 km thick porous megaregolith layer (Murphy Quinlan et al., 2021a,b). The core-mantle boundary (CMB) and residence depth of the Imilac pallasite meteorite (61 km, from metal cooling rates; Murphy Quinlan et al., 2021a) are labelled. (b) Temperature profile at this 61 km depth, and temperature difference across a 400 m slice of mantle centred at this depth ($\Delta T = |T_b - T_t|$). These outputs provide the initial and boundary conditions for the intrusion model. The blue vertical line shows the time of intrusion of metal into the mantle (chosen), while the purple dashed line shows the time metallographic cooling was recorded in the pallasite sample (measured). (c & d) Initial conditions for the intrusion model: two 2D slices through the 3D ellipsoid geometry (prolate ellipsoid). Z lies along the planetesimal radius, and shows the vertical temperature gradient, while X and Y have constant temperature. The blue ellipsoid represents the intrusion region, with a temperature of 1660 K.

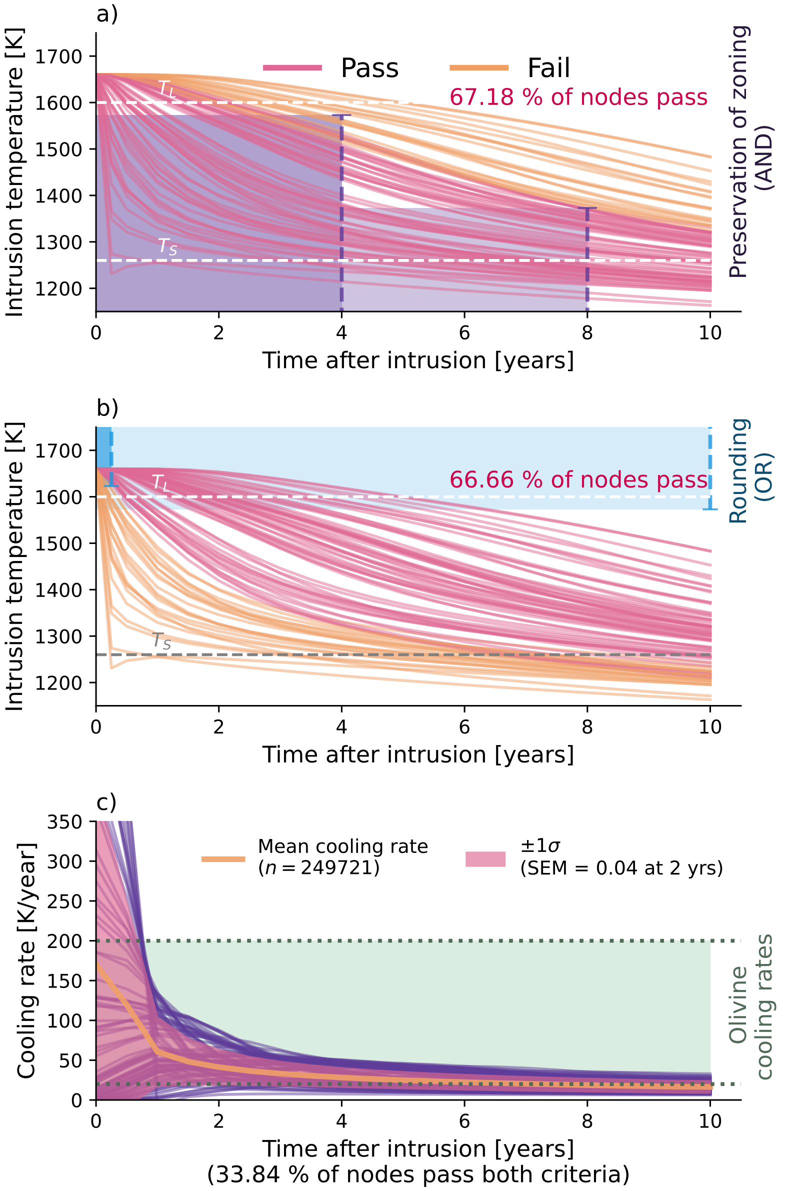

Figure 3: Results and output for a single model run with initial conditions in Figure 2. Each line is a temperature or cooling rate time-series for a volume element within the intrusion described in Figure 2 (e.g. within the blue ellipsoid). Each model is initially assigned a score of zero. Panel (a) shows a sample of nodes (200) within the intrusion filtered according to whether olivine zoning would be preserved at that location. If the model “passes” the zoning preservation criteria (≥ 50 % of points will preserve zoning, as is true in this example with 67.2 % passing), one is added to the model’s score. Panel (b) shows the same nodes filtered according to whether olivine grains will be microscopically rounded at that location. If the model “passes” the olivine rounding criteria (≥ 50 % of points will round olivine, as is true in this example with 66.7 % of nodes passing), one is added to the model’s score. A score of two is deemed “successful”. The full array of nodes within the intrusion area is used to calculate these percentages (108,737 in this example). Panel (c) shows the cooling rates for the same selection of nodes. The mean cooling rate and standard deviation were calculated with all nodes in the intrusion ellipsoid (108,737 voxels in this example). The green shaded region highlights the range of cooling rates suggested by Miyamoto (1997) to explain pallasite olivine zoning.

Each node within the intrusion region was filtered as described in section 3.3, and the volume percentage of the intrusion meeting the rounding requirements and zoning requirements were calculated independently (Figure 3). Approximately 67 % of the intrusion region cools quickly enough to preserve calcium zoning in olivine (Figure 3 a), passing the requirement of ≥ 50 % by volume of the intrusion region meeting the zoning criterion. The rounding requirement is also met by just under 67 % of nodes in the intrusion region, passing the requirement of ≥ 40 % by volume of the region meeting this criterion. The model receives a score of two, indicating that it meets both requirements.

This result demonstrates that an ellipsoidal intrusion of molten metal into a porous olivine planetesimal mantle can reproduce the necessary thermal evolution pathways both to facilitate the rounding of small olivine grains, and to allow the preservation of Ca zoning. Within the intrusion region, mean cooling rates of $\sim$ 10–150 K/year are reached, agreeing with the elevated cooling rates suggested by Miyamoto (1997) to explain olivine diffusion profiles (Figure 3 c). This model also agrees with recorded metal cooling rates due to the initial and boundary conditions; once the intrusion cools to the background mantle temperature (15 – 50 years by conductive cooling, depending on size of the intrusion), it will continue to cool at the same rate as the planetesimal mantle, and will cool through the required temperature window at the rate predicted by metal cooling rates (Bryson et al., 2015; Yang et al., 2010; Murphy Quinlan et al., 2021a).

5 Exploring the parameter space

In order to explore how commonly pallasite formation models can yield conditions that preserve the disparate cooling rates, the model procedure was repeated for different intrusion times in the 250 km radius planetesimal (300 models), and for a 300 km radius planetesimal with a 250 km radius core, and an 8 km megaregolith layer (300 models, reproducing a case from Nichols et al., 2021) with randomised intrusion geometry allowing the unique and non-unique axes of the ellipsoid to vary and change orientation, to produce vertically and horizontally oriented sheets (dike and sill-like) and pipes. Randomised initial mantle temperatures were also chosen to approximate different parent body geometries and a range of different intrusion depths (600 models). The summarised results of these 1200 model runs are shown in Figure 4, and ranges within which parameters were varied in Table 1. We also ran a suite of 1000 models with varying material properties including density, heat capacity, and crystallisation temperature in addition to randomly selected mantle temperatures and intrusion geometry, which allowed us to approximate the effect of adding a small percentage of trapped metal to the mantle or changing the composition of the intruding metal, as well as testing the model's sensitivity to these parameters.

Neither initial intrusion temperature (Figure 4, third column) nor metal fraction (by volume, Figure 4, fourth column) strongly control whether the intrusion region will match both constraints. Intrusion volume is a strongly controlling parameter (Figure 4, first column), with the majority of models with a volume smaller than 5×10^5 and greater than 5×10^6 m^3 meeting only one constraint. Smaller volumes favour rapid cooling and preservation of zoning, while larger intrusions favour rounding of olivine grains due to their protracted cooling. While background mantle temperature displays a weak negative relationship with the overall model score, it is strongly negatively correlated with zoning preservation, and moderately positively correlated with rounding potential (Figure S7). Cooler mantle background temperatures (Figure 4, second column) result in higher mean cooling rates and favour meeting both constraints (Figure 4n). These trends hold true not only for model results that use mantle temperature inputs from the planetesimal model, but also for the randomised input parameters that cover a larger parameter space, when material properties are varied randomly (Figure S8), when different volume % requirements are used (Figure S9), and in the more specific sensitivity tests (Table S1, Figures S8, S10, S11).

Varying the trapped metal content in the mantle or the mantle diffusivity does not systematically change the mean intrusion temperature after ten years, the zoning preserved or the rounding expected (Figure S12), with no significant correlation found between either olivine or metal material properties and model results (Figure S14).

Based on the mean temperature of the intrusion through time, we calculated the mean cooling rate and average temperature of the intrusion between three months and ten years; this allows for an approximate overview of the cooling rate over the model run time, excluding the extremely rapid cooling on initiation of the model. Figure 5 highlights the temperatures and cooling rates relevant to rapid pallasite olivine cooling

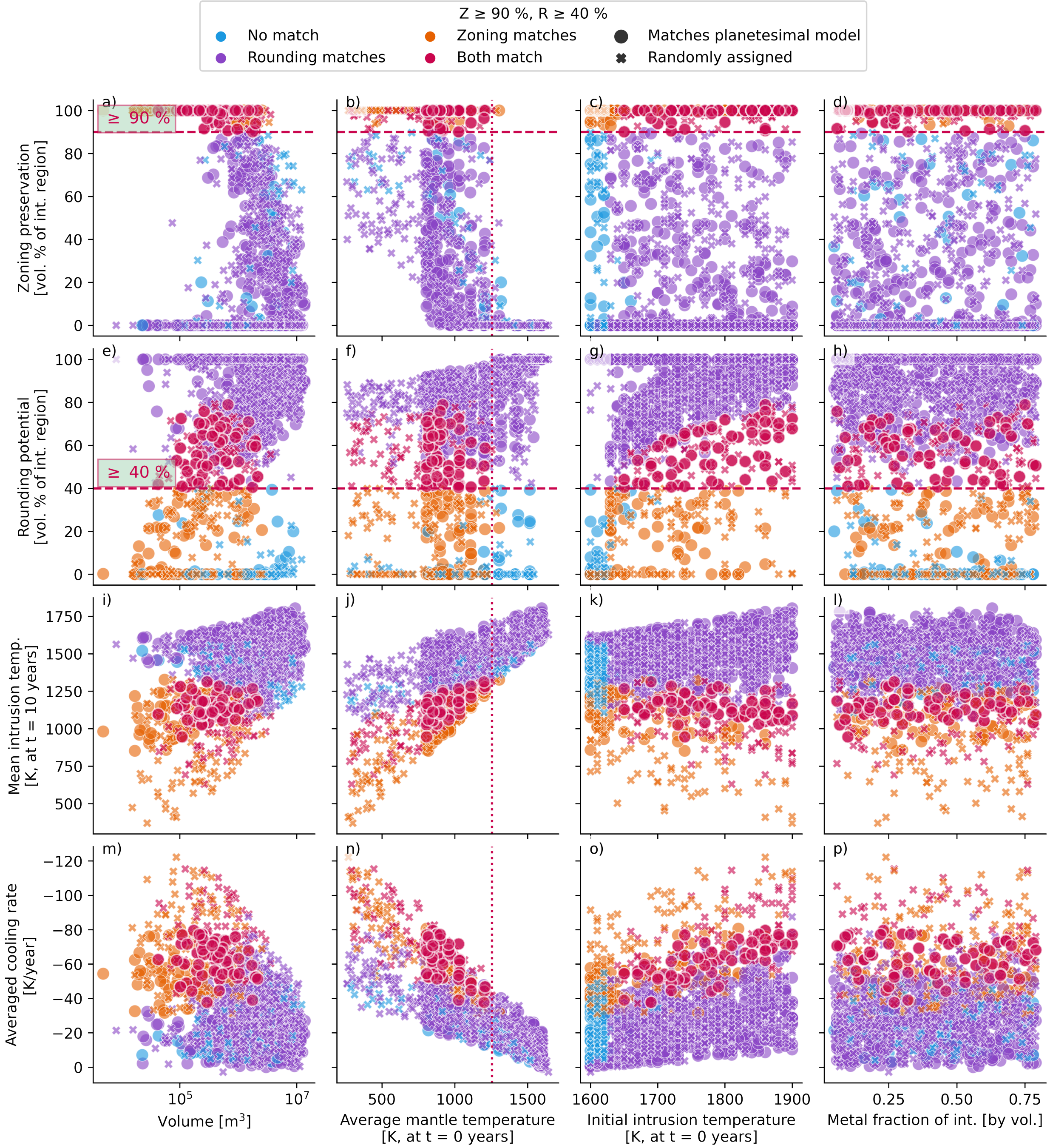

Figure 4: Summary of results for 1200 model runs with constant material properties. Colour denotes which constraints were matched: blue means neither constraint was matched, pink—that both were matched, orange—zoning constraint was matched, and purple—rounding constraint matched. Marker shape describes the initial temperature conditions: either output from a planetesimal model, or randomly assigned. Parameters were not varied in isolation. Large pink circles match both constraints and used input from a planetesimal model.

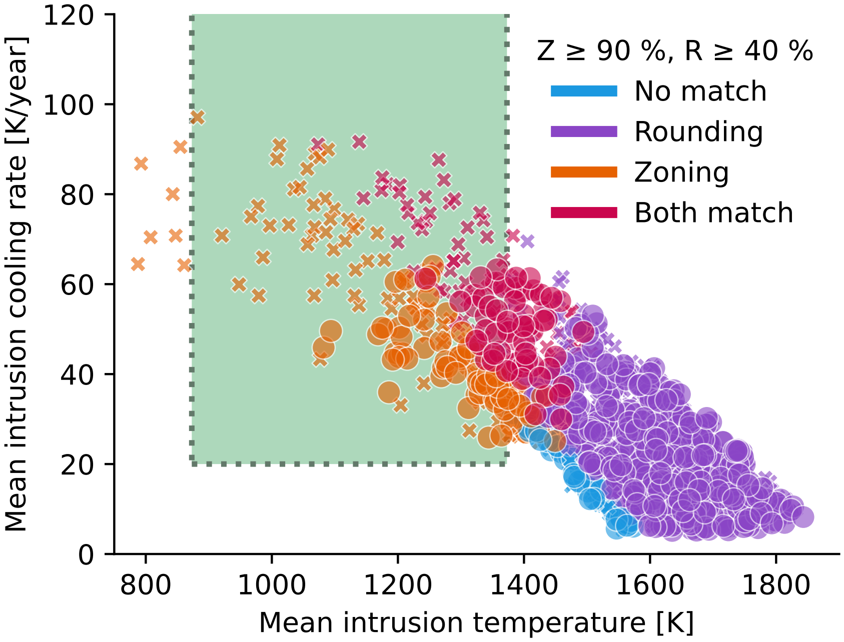

Figure 5: Mean intrusion temperatures and cooling rates over the model run time (from 3 months to 10 years) for the intrusion region for 1200 model runs with constant material properties. The shaded region highlights the cooling rates and temperatures suggested by Miyamoto (1997), estimated from olivine diffusion profiles (Hsu, 2003). Model results that fall within this region reproduce the required rapid cooling in the relevant temperature window. Colour denotes which constraints were matched: blue means neither constraint was matched, pink—that both were matched, orange—zoning constraint was matched, and purple—rounding constraint matched. Marker shape describes the initial temperature conditions: either output from a planetesimal model (filled circles), or randomly assigned (“x” symbols).

suggested by Miyamoto (1997); sufficiently high cooling rates are reached in the first few years of cooling. This suggests that both short-term, rapid cooling of olivine in molten metal, followed by much slower cooling of the FeNi metal, are explained by the intrusion of hot metal into a warm mantle.

We additionally tested a range of filter requirement pairs, to investigate how dependent on our filter cut-off limits our results were (parentheses show the shorthand used in Figure S9):

- Zoning $\geq$ 30 vol. %, rounding $\geq$ 30 vol. % (Z $\geq$ 30 %, R $\geq$ 30 %)
- Zoning $\geq$ 50 vol. %, rounding $\geq$ 50 vol. % (Z $\geq$ 50 %, R $\geq$ 50 %)
- Zoning $\geq$ 70 vol. %, rounding $\geq$ 70 vol. % (Z $\geq$ 70 %, R $\geq$ 70 %)
- Zoning $\geq$ 90 vol. %, rounding $\geq$ 70 vol. % (Z $\geq$ 90 %, R $\geq$ 70 %)

Generally, the overall same trends are seen across these results as in our default filter pair (Z $\geq$ 90 %, R $\geq$ 40 %) with higher intrusion temperatures and smaller mean intrusion radii favoured as the filter requirements increase (Z $\geq$ 70 %, R $\geq$ 70 %). The correlation of overall model score and background mantle temperature is more strongly negative when both filters are low (Z $\geq$ 30 %, R $\geq$ 30 %), with the correlation weakening as both filters increase and the total number of models that fit both constraints reduces (Figure S15).

6 Discussion

A simple model of a metallic intrusion into the mantle of a planetesimal reproduces the gross statistical properties of olivine texture and diffusive modification observed in pallasite meteorites, and replicates the contrasting slow metal and rapid olivine cooling rates estimated from various elemental diffusion profiles. This model reproduces these results without the need for impact-exhumation or parent body break-up to explain rapid olivine cooling rates, or the addition of a late thick megaregolith layer to explain slow cooling, as have been invoked by previous models (Yang et al., 2010; Bryson et al., 2015; Walte et al., 2020; Walte and Golabek, 2022).

Walte and Golabek (2022) list the observational constraints from pallasite samples that formation models much match, comprising: remnant magnetisation, a warm mantle prior to pallasite formation, rapid cooling at high temperatures (>1200 K), slow cooling at lower temperatures (1000–700 K), varied residence depths (from metal cooling rates), and low Ir concentrations implying differentiation of the injected molten metal. Their qualitative model of a non-destructive two-body collision agrees with all the available constraints; however, it requires impact rebound or a similar effect to produce rapid cooling after impact and development of a megaregolith layer to support later slow cooling (Walte et al., 2020). Our planetesimal model assumes either disruption and re-accretion of the same thickness of regolith during and after impact, or no impact-related disruption; however, our results are not dependent on the presence of a regolith layer (Figure S16). We show quantitatively that an intrusion of molten metal into a planetesimal mantle can meet the above constraints without the need for an impact rebound or development of a late thick megaregolith layer to slow cooling. While our results do not preclude large-scale changes to the parent body, it removes the need for them; this means that future work can seek lines of evidence for these planetary-scale processes instead of them being assumed a requirement for pallasite formation.

We show that the required criteria for pallasite formation can be met for a wide range of intrusion morphologies (Figure 6d), at a wide range of mantle temperatures (as a proxy for both timing of intrusion and residence depth). For models using planetesimal mantle temperature as initial conditions, criteria were met more often later in the planetesimal's history (shortly before the slow metal cooling rates were recorded), when the mantle was cooler and faster intrusion cooling rates could be achieved (Figure 6a, b); the zoning preservation requirements cannot be met unless the temperature of the mantle is at or below 1373 K, as the intrusion needs to cool below this temperature within 8 years.

Small intrusion regions with mean radii between 20 and 100 m produce the rapid cooling required to preserve olivine chemical heterogeneity (Figure 6c). Similarly, high aspect ratio morphologies (more pipe- or sheet-like) with a minimum radius < 50 m more frequently meet the constraints as opposed to intrusion segments that are more spherical in shape with both maximum and minimum radii above $\sim$ 50 m (Figures 6d, S13), with a weak non-monotonic correlation measured (Figure S7). This suggests that pallasite-material

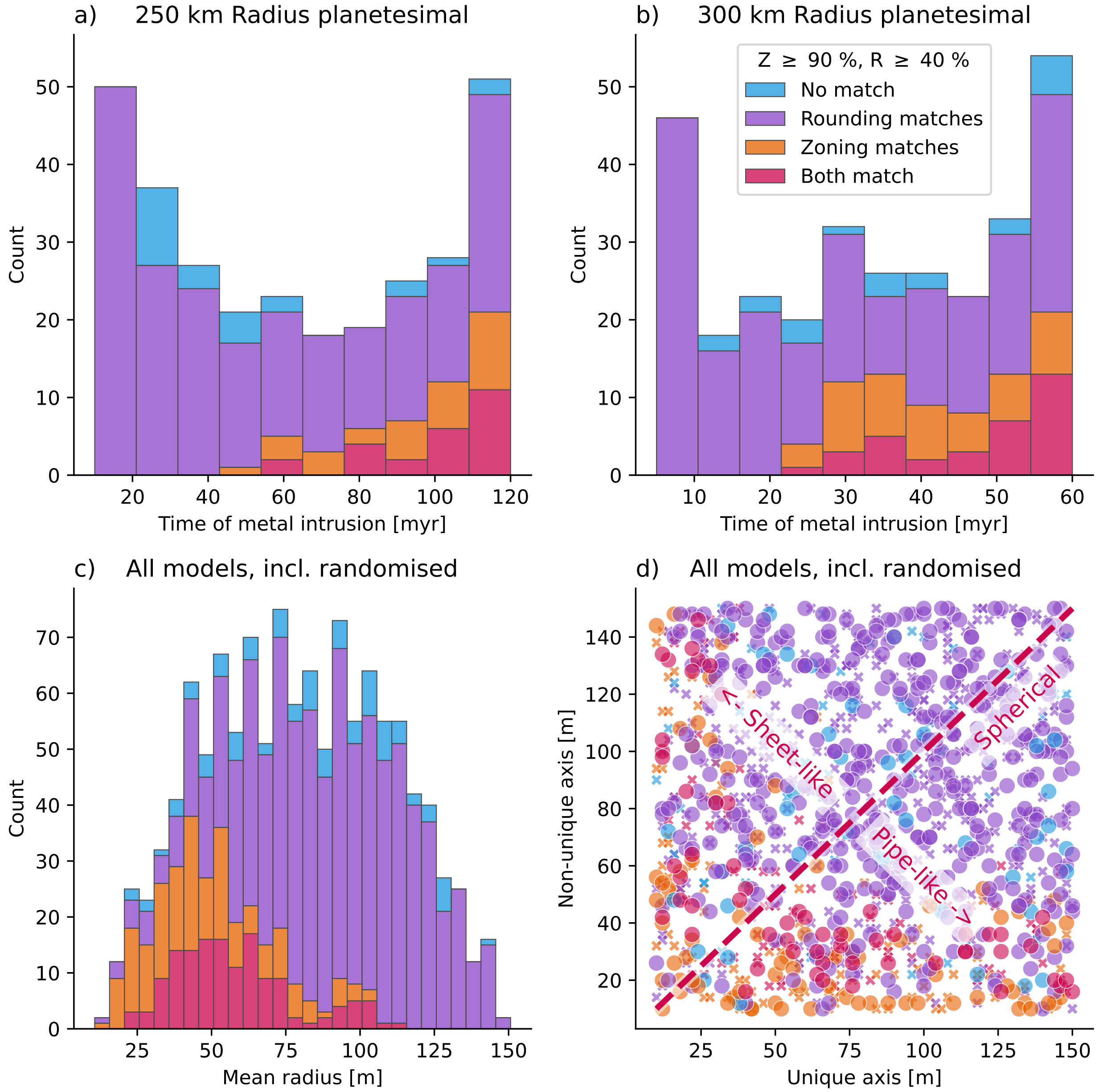

Figure 6: Dependence of model outputs on timing of intrusion, volume of intrusion region, and geometry of intrusion region. a & b) Histograms of score for timing of metal intrusion (in millions of years after initiation of model/crystallisation of magma ocean) for both planetesimal models (299 and 301 models respectively). Maximum time on both histograms is the time the metal cooling rate was recorded. c) Histograms of model outputs for mean radius of intrusion region for all models with constant material properties (1200 model runs). d) Dependence of model outputs on intrusion region volume and aspect ratio for all models with constant material properties (1200 model runs).

formation is constrained to intrusions with a sufficiently small minor axis (of ~ 50 m). When the minimum volume fraction requirement of either rounding or zoning in the intrusion region is increased (thus allowing fewer models to pass), this effect becomes more pronounced with a smaller range of radii resulting in both constraints being met (Figure S17).

In our implementation, the volume of the intrusion region required to satisfy the rounding criteria is set arbitrarily at ≥ 40 vol. %, as a detailed systematic study of micro-scale rounding is not available in the literature. We neglect the effect of varying metal/olivine proportion in samples (and their source region of the intrusion), varying local sulfur content, and localised chemical or deformation events. Despite these limitations, our model shows that parameters such as the metal fraction of the pallasite region and the proportion of metal trapped in the planetesimal mantle do not systematically change whether pallasite-like material can be produced. Our results also highlight the importance of the timing of metal intrusion into the parent body mantle, and the temperature at which the intruded mantle is residing. Changing the proportion or volume percentage of rounding required even by a significant percentage does not change the conclusions of our study within the parameter range explored: that rounded olivine and preserved chemical zoning can be recovered from the same pallasite intrusion volume.

Hsu (2003) describes calcium zoning in pallasite olivine as ubiquitous, which in combination with detailed diffusion of Ca in olivine studies, makes it a sensible choice for first steps in calculating erasure or preservation potential in a metallic intrusion. We set the zoning preservation requirement to $\geq 90\%$, implying that essentially all pallasites must preserve some degree of Ca heterogeneity while allowing for some uncertainty. However, we also considered lower requirements of ≥ 30 %, ≥ 50 %, and ≥ 70 % to allow regions of erasure and more intensive diffusional modification (see Figure S9). Lowering both the zoning and rounding requirements to ≥ 30 % increased the number of model runs that meet both constraints from 276 (12.55 % of 2200 model runs) to 506 (23.00 % of 2200; see Tables S2, S3). The same dependence on mantle temperature and intrusion volume is seen and rapid olivine cooling rates are still met between four and eight years after intrusion (Figure S8) .

As mentioned previously, the time and temperature pairings used to estimate grain rounding and zoning preservation are associated with large and unquantifiable errors. In order to assess the sensitivity of the model to the temperature requirements, we varied the temperature of each filter by ±10 % of the original temperature (Table S2, Figures S18, S19). While the absolute number of successful models changed, the overall relationship between model score and parameters such as initial temperature, background mantle temperature or intrusion volume remained essentially the same (Figure S17). We also assessed the change through time in intrusion volume that satisfies each temperature requirement, for the example model run illustrated in Figure 3. We found that the rounding requirement of $T_{\text{3mnths}} \geq 1623\,\text{K}$ was most strongly dependent on timing of the measurement, as the intrusion is still rapidly cooling at this time. The intrusion region satisfying this requirement will change by approximately ±10 vol. % per month at this stage in the intrusion process (Figure S4), whereas by four, eight and ten years when the other temperature requirements must be matched, the change in the intrusion region that matches each constraint is ~ 1 vol. % or less per month. At three months, changing the temperature requirement by ±10 % may result in a model no longer passing the rounding criterion (Figure S4); however, this does not change the overall relationship between the input parameters and the results (Figure S17).

The inclusion of a fraction of metal within the planetesimal mantle may explain the presence of large (radius ~ 5 mm), well rounded olivine crystals: Saiki et al. (2003) estimated that olivine grains with a radius of 5 mm would be fully rounded in the presence of FeNi after 7 Myr at or above 1673 K, 29 Myr at or above 1573 K, or 241 Myr at or above 1473 K. This is significantly slower than the experimental rounding results of Walte et al. (2020) when the empirical equation of Saiki et al. (2003) is scaled down to the same size fraction of olivine grains; potentially due to experimental design and the absence of sulfur which has been shown to accelerate rounding (Solferino et al., 2015; Solferino and Golabek, 2018), and so these temperature and time constraints can be treated as upper bounds. While we primarily focus on models of the pallasite parent body with a purely olivine mantle, we also modelled a parent body with 15 vol. % metal trapped in the mantle, representing the upper limit of primary metal fraction observed in Seymchan in Walte et al. (2020) (note that Scott (2017) suggests a higher original primary metal fraction for large round-type pallasites such as Brenham, approximately 30 vol. %; Walte and Golabek, 2022). We assumed that the sole effect of adding this small fraction of metal is to increase the mantle diffusivity, which in turn accelerates planetary-scale cooling by a small degree (Figure 7). We find that hotter mantles (post magma ocean solidification, with higher

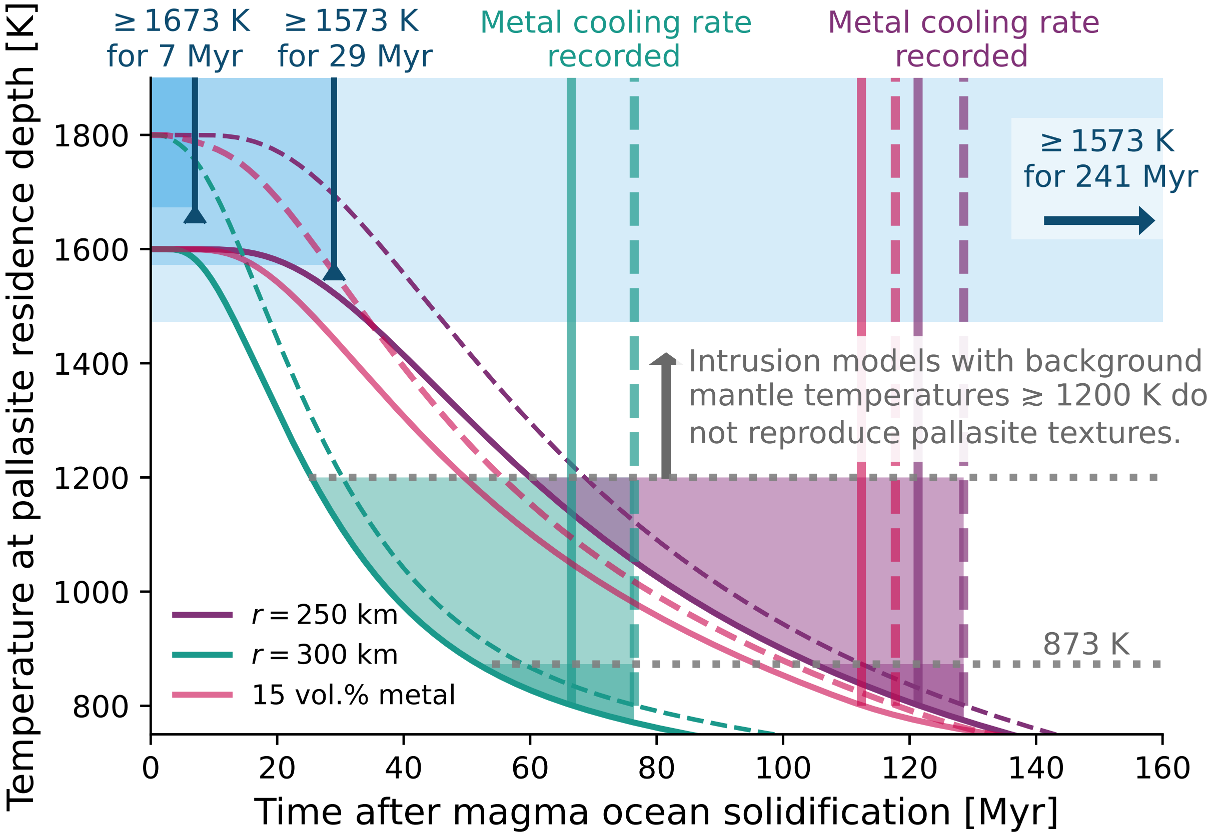

Figure 7: Temperature time series at depth of Imilac pallasite residence, based on FeNi cooling rates (Yang et al., 2010), for a 250 km radius planetesimal with a 125 km radius core (Murphy Quinlan et al., 2021a), a 300 km radius planetesimal with a 200 km radius core (Nichols et al., 2021), and a a 250 km radius planetesimal with a 125 km radius core, and 15 % by volume metal trapped in the mantle. Blue boxes represent temperature criteria suggested by Saiki et al. (2003) to explain rounding of large (5 mm radius) olivine crystals; the model cooling time series must pass through one of the blue lines. The two horizontal grey dashed lines indicate maximum background mantle temperature at time of final metal intrusion to meet different criteria: in order to preserve Ca zoning, background mantle temperature must be below 1200 K, which in order to cool through temperature window at the cooling rates suggested by Miyamoto (1997), the background mantle temperature must be below 873 K.

olivine solidus temperatures) better facilitate this large-scale, long term rounding of olivine grains (Figure 7). We also varied the metal content in the mantle region surrounding the intrusion in our intrusion-scale model between 0–20 vol %, but found no systematic effect on the score of models (Figure S12).

While hotter initial mantle temperatures are required for this earlier period of olivine rounding, the final stage of metal intrusion that is recorded in pallasites was most likely injected into a cooler mantle that was approaching ~ 800 K (Figure 6 a, b, Figure 7). We find that intrusions of all sizes into mantles of ~ 1250 K and hotter rarely cool below 1373 K quickly enough to preserve Ca zoning in large volumes of the intrusion region (Figures 4, 7). In order to reproduce the cooling rates through 873 K suggested by Miyamoto (1997), the background mantle must be below this temperature at the time of intrusion (Figure 7). This restricts the timing of the pallasite-forming metal intrusion to between $\sim$ 10–30 Myr before cooling through the metallographic cooling rates at approximately 800 K; for planetesimal models similar to those of Tarduno et al. (2012), Bryson et al. (2015), Solferino and Golabek (2018), Nichols et al. (2021), or Murphy Quinlan et al. (2021a), this suggests intrusion occurred tens of millions of years after the formation of the parent body.

Interestingly, Mn-Cr isotope systematics may suggest a more rapid parent-body evolution: Windmill et al. (2022) argue that the pallasite region of the mantle must have cooled below the Mn-Cr closure temperature ($\sim$1000 °C, 1273 K) within 10 million years of Solar System formation (CAI condensation). This requires a rapidly cooling parent body, orders of magnitude faster than suggested by the planetesimal models listed above(Tarduno et al., 2012; Bryson et al., 2015; Solferino and Golabek, 2018; Nichols et al., 2021; Murphy Quinlan et al., 2021a), and additionally necessitates the intrusion of bolide-sourced metal before 10 million years after CAI formation. This early timing of metal injection is also supported by the isotopic studies of Kruijer et al. (2022) who find a genetic link between pallasite meteorites and the IIIAB irons, and link the chronology of pallasite formation and metal intrusion to the breakup and core exposure of the IIIAB parent body.

There are a few key differences in the assumptions in the modelling approach taken here and in Windmill et al. (2022): firstly, we assume that the rapid cooling (K/year) experienced by pallasite olivine records a localised reheating and subsequent rapid cooling due to metal injection into the mantle, whereas Windmill et al. (2022)assume that this is representative of overall planetary cooling; secondly, we use slow metal cooling rates (K/Myr) to constrain the planetary cooling, while Windmill et al. (2022) do not reconcile these with the rapid cooling in their exponential cooling rate.

These results are not incompatible with our model, but they do require that the early planetesimal cooling in the region of pallasite formation is accelerated with respect to our parent body model, essentially compressing the timeline illustrated in Figure 7. While this does not agree with our default planetesimal models, this can be achieved by reducing the parent body radius, thinning or removing the regolith layer, or by increasing the core fraction to create a thin-mantled planetesimal as in Nichols et al. (2021), resulting in shallower pallasite residence depths (Figure S16, Tables S4, S5). As noted previously, few models with background mantle temperatures above approximately 1250 K preserve zoning in large volume fractions of the intrusion region (see also Tables S6 and S7), and so a less restrictive zoning preservation constraint is required.

Our simple model could be developed by incorporating more complex grain-growth and rounding mechanisms, such as that of Solferino and Golabek (2018), which focuses on olivine grain growth in contact with Fe-Ni-S at different depths within a planetesimal mantle. While we take a macroscopic approach to modelling the olivine-metal mixing region, a micro-scale investigation of the crystallisation of metal in contact with olivine and the potential volume change, localised reactions textures and microstructures would provide further constraints on the pressure, temperature and time of mixing between these phases.

An interesting area of research outside the scope of the current study is the details of metal intrusion into the parent body mantle and the dominant mode of transport of the metal through the mantle. While previous models have suggested that the metal may have an internal source (eg., the molten core of the planetesimal, suggested by a ferrovolcanism origin; Johnson et al., 2020), recent isotopic studies show a statistically significant disequilibrium between the metal and silicate phases in pallasites, strengthening the argument for an external source delivered via impact (Bennett et al., 2022; Windmill et al., 2022). Studies of core formation via percolative flow (Solferino et al., 2020; Berg et al., 2018) and intrusion propagation and emplacement (Walker et al., 2021; Stephens et al., 2021) alongside microstructural evidence from pallasite samples can be utilised to better understand this. Our model can aid in this research, as it provides a range of mantle temperatures over which pallasite-like textures can be produced.

Instead of attempting to recover specific details of the pallasite parent body, we have taken a statistical approach to constrain the range of parameters over which pallasite formation is possible. Our results show that the development of conditions favourable to pallasite formation are common across the parameters we tested, but are constrained by the mantle temperature, which can be considered a proxy for the timing of metal intrusion. The two-stage formation hypothesis of Walte and Golabek (2022) suggests that an earlier impact injected metal into the pallasite parent body mantle, but did not produce "pallasite-like textures" as observed in meteorite samples, because the mantle was too hot at the time. Instead, the region of intrusion achieved textural equilibrium, only retaining a small fraction of metal in contact with rounded olivine grain boundaries. A later impact is proposed to then deliver more molten metal into the cooler mantle, producing the textures observed in samples. Our model reproduces the timescales suggested by both these different stages of formation. These metal-injection events may be a recurrent stage in planetesimal development, representing a halted core-growth event where cooler mantle temperatures do not facilitate migration of metal all the way to the centre of the planetesimal before solidification.

Framed in this way, perhaps the unusual feature of pallasite meteorites is that they were excavated in such a way that preserved them and allowed them to be delivered to Earth, as opposed to their formation being a unique event. This is supported by the evidence for planetesimal growth in two distinct reservoirs in our Solar System (Morbidelli et al., 2022), both of which are sampled by pallasitic material: while we specifically discuss and model the parent body of the Main Group Pallasite meteorites, the umbrella group of pallasites including the Eagle Station Pallasites, the Pyroxene Pallasites, and anomalous ungrouped samples, must sample multiple parent bodies sourced from both the carbonaceous and non-carbonaceous reservoirs (Jacquet, 2022). These similar lithologies, samples from different regions of the early Solar System, from isolated planetesimals, suggests that this process was repeated on multiple bodies. Jacquet (2022) suggests a renaming of the pallasite class to "dunite-iron" meteorites to highlight the textural similarities instead of inferring a genetic link.

It is possible that multiple metal impacts delivered metal to the mantle of the pallasite parent body over the course of its life span: some of which may have supported core growth during the magma ocean stage of differentiation; others which stalled in the hot, newly-solidified mantle and eventually reached textural equilibrium, producing regions of well-rounded, large olivine grains; and later still an intrusion into a cooler mantle that facilitated rounding of some smaller olivine grains fractured during intrusion, preservation of chemical heterogeneity in areas previously untouched by prior intrusions, and rapid heating, cooling, and subsequent diffusional modification of olivine rim compositions. Following this intrusion, the body continued to cool, the core crystallised and paleomagnetism was recorded in some samples (Bryson et al., 2015; Nichols et al., 2021; Murphy Quinlan et al., 2021a), and the body became geologically frozen in place until its destruction $\sim$ 100 Myr ago (Herzog et al., 2015).

7 Conclusions

Different formation environments are not required to explain varied levels of rounding of olivine grains in pallasite meteorites: large, well-rounded grains may predate metal intrusion and be linked to contact with primordial metal pockets (Walte et al., 2020) or an earlier injection of metal into a hotter planetesimal mantle (Walte and Golabek, 2022), while angular olivines were derived from dunite aggregates that contained no or less primary metal. Fragmental grains may have been fractured during metal intrusion. All grains in the intrusion region then were rounded microscopically according to their location in the intrusion - grains near the periphery would have cooled rapidly and preserve their initial state without microscopic rounding of corners (whether macroscopically well-rounded, fragmental, or angular), while olivine grains nearer the centre of the intrusion region would cool more slowly, resulting in micro-scale rounding of corners.

Large-scale disruption of, or accretion to, the pallasite parent body are not required to reproduce the contrasting cooling timescales suggested by olivine and metal diffusion. Instead, the rapid injection of hot metal into a slowly cooling, warm planetesimal mantle creates a temperature perturbation leading to rapid initial cooling in the local area, matching that required to preserve olivine compositional heterogeneity, followed by equilibration with the mantle and a return to the slow planetesimal-scale cooling rates recorded in the Ni diffusion profiles in the Widmanstätten texture. While Walte and Golabek (2022) suggest that the pallasite-forming metal intrusion event was aided by still-molten trapped metal pockets, residing in a parent-body mantle above the metal solidus, the later impact and large scale injection of metal could have re-melted these preexisting FeNi pockets locally, enabling impact into a marginally cooler mantle.

Within one small ellipsoidal segment of intrusion, a diversity of textural and diffusive modification of olivine can be achieved. This does not preclude different formation environments for pallasite meteorites with differing olivine textures or diffusion profiles, rather it removes this as a requirement. Our simple model shows that further understanding of the small-scale processes related to the mixing of olivine and metal in the pallasite region is required to understand the planetesimal-scale processes. The model also highlights the importance of the temperature of the mantle on the evolution of the pallasite region, and how this is linked to relative timing of the injection of metal following the crystallisation of the magma ocean, and shows how different regions of one small intrusion can experience very different temperature-time paths.

We produced a simple, first-step model to address the contrasting timescales preserved in pallasite meteorites and suggest that the simplest explanation (injection of metal into the mantle of a planetesimal) without ad hoc changes to the parent body, can explain the heterogeneity seen across pallasite meteorites. We suggest that pallasite meteorites represent a late, preserved metallic intrusion into a planetesimal mantle and speculate that this parent body potentially experienced earlier metal-injections: previous intrusions would have delivered material to the core, leaving a small fraction trapped within the mantle.

Acknowledgements

M. Murphy Quinlan was supported by the Leeds-York Natural Environment Research Council Doctoral Training Partnership (NE/L002574/1). C. J. Davies was supported by Natural Environment Research Council Grant (NE/V010867/1). We would like to thank our reviewers, Nicolas P. Walte and Fakhri Bintang, for taking the time to produce detailed and helpful reviews, and for providing comments, insights and suggestions that improved the quality of this manuscript.

Pytesimal v2.0.0 (Murphy Quinlan et al., 2021b) was used to model the thermal evolution of the parent body, and PytesiMINT v0.1.0 (Pytesimal Metal INTrusion; Murphy Quinlan, 2023) was used to model the mixed-phase metal intrusion region, both of which are built in Python (Python Software Foundation, https://www.python.org/) and make use of the following open-source libraries: Numpy (Harris et al., 2020); Matplotlib (Hunter, 2007); SciPy (Virtanen et al., 2020); Numba (Lam et al., 2015); and pandas (McKinney, 2010).

References

N. Bennett, C. Sio, E. Schauble, C. Lesher, J. Wimpenny, and A. Shahar. Iron isotope evidence of an impact origin for main-group pallasites. *Geochemical Perspectives Letters*, 23:6–10, sep 2022. doi: 10.7185/geochemlet.2229. URL `https://doi.org/10.7185/geochemlet.2229`.

M. T. L. Berg, G. D. Bromiley, Y. Le Godec, J. Philippe, M. Mezouar, J.-P. Perrillat, and N. J. Potts. Rapid core formation in terrestrial planets by percolative flow: In-situ imaging of metallic melt migration under high pressure/temperature conditions. *Frontiers in Earth Science*, 6:77, Jun 2018. doi: 10.3389/feart.2018.00077. URL `https://www.frontiersin.org/article/10.3389/feart.2018.00077/full`.

J. S. Boesenberg, J. S. Delaney, and R. H. Hewins. A petrological and chemical reexamination of main group pallasite formation. *Geochimica et Cosmochimica Acta*, 89:134–158, July 2012. doi: 10.1016/j.gca.2012.04.037. URL `https://doi.org/10.1016/j.gca.2012.04.037`.

J. F. J. Bryson, C. I. O. Nichols, J. Herrero-Albillos, F. Kronast, T. Kasama, H. Alimadadi, G. van der Laan, F. Nimmo, and R. J. Harrison. Long-lived magnetism from solidification-driven convection on the pallasite parent body. *Nature*, 517(7535):472–475, 2015. doi: 10.1038/nature14114.

P. R. Buseck. Pallasite meteorites — mineralogy, petrology and geochemistry. *Geochimica et Cosmochimica Acta*, 41(6):711–740, 1977.

H. S. Carslaw and J. C. Jaeger. *Conduction of heat in solids.* Clarendon Press ; Oxford University Press, Oxford : New York, 2nd edition, 1959.

W. Cen, R. Hoppe, and N. Gu. Fast and accurate determination of 3D temperature distribution using fraction-step semi-implicit method. *AIP Advances*, 6(9):095305, 2016. doi: 10.1063/1.4962665.

S. M. Chernonozhkin, S. J. McKibbin, S. Goderis, S. J. M. Van Malderen, P. Claeys, and F. Vanhaecke. New constraints on the formation of main group pallasites derived from in situ trace element analysis and 2D mapping of olivine and phosphate. *Chemical Geology*, 562:119996, 2021. doi: 10.1016/j.chemgeo.2020.119996.

J. Crank and P. Nicolson. A practical method for numerical evaluation of solutions of partial differential equations of the heat-conduction type. *Mathematical Proceedings of the Cambridge Philosophical Society*, 43(1):50–67, 1947. doi: 10.1017/s0305004100023197.

E. G. Ehlers. *The Interpretation of Geological Phase Diagrams.* W. H. Freeman and Co., Ltd., 1972.

J. I. Goldstein, J. Yang, and E. R. Scott. Determining cooling rates of iron and stony-iron meteorites from measurements of Ni and Co at kamacite–taenite interfaces. *Geochimica et Cosmochimica Acta*, 140:297–320, 2014. doi: 10.1016/j.gca.2014.05.025. URL `https://linkinghub.elsevier.com/retrieve/pii/S0016703714003548`.

J. Grossman and Nomenclature Committee of the Meteoritical Society. Meteoritical Bulletin Database. https://www.lpi.usra.edu/meteor/, 2022. Accessed: 2022-02-26.

C. R. Harris, K. J. Millman, S. J. van der Walt, R. Gommers, P. Virtanen, D. Cournapeau, E. Wieser, J. Taylor, S. Berg, N. J. Smith, R. Kern, M. Picus, S. Hoyer, M. H. van Kerkwijk, M. Brett, A. Haldane, J. F. del Río, M. Wiebe, P. Peterson, P. Gérard-Marchant, K. Sheppard, T. Reddy, W. Weckesser, H. Abbasi, C. Gohlke, and T. E. Oliphant. Array programming with NumPy. *Nature*, 585(7825):357–362, Sept. 2020. doi: 10.1038/s41586-020-2649-2. URL `https://doi.org/10.1038/s41586-020-2649-2`.

G. F. Herzog, D. L. Cook, M. Cosarinsky, L. Huber, I. Leya, and J. Park. Cosmic-ray exposure ages of pallasites. *Meteoritics & Planetary Science*, 50(1):86–111, 2015. doi: 10.1111/maps.12404. URL `https://onlinelibrary.wiley.com/doi/abs/10.1111/maps.12404`.

W. Hsu. Minor element zoning and trace element geochemistry of pallasites. *Meteoritics & Planetary Science*, 38(8):1217–1241, 2003. ISSN 10869379, 19455100. doi: 10.1111/j.1945-5100.2003.tb00309.x.

J. D. Hunter. Matplotlib: A 2d graphics environment. *Computing in Science & Engineering*, 9(3):90–95, 2007. doi: 10.1109/MCSE.2007.55.

E. Jacquet. Meteorite petrology versus genetics: Toward a unified binominal classification. *Meteoritics & Planetary Science*, 57(9):1774–1794, 2022. doi: https://doi.org/10.1111/maps.13896.

B. C. Johnson, M. M. Sori, and A. J. Evans. Ferrovolcanism on metal worlds and the origin of pallasites. *Nature Astronomy*, 4(1):41–44, 2020. doi: 10.1038/s41550-019-0885-x. URL `http://www.nature.com/articles/s41550-019-0885-x`.

A. J. G. Jurewicz and E. B. Watson. Cations in olivine, Part 2: Diffusion in olivine xenocrysts, with applications to petrology and mineral physics. *Contributions to Mineralogy and Petrology*, 99(2):186–201, 1988. doi: 10.1007/BF00371460.

T. S. Kruijer, C. Burkhardt, L. E. Borg, and T. Kleine. Tungsten and molybdenum isotopic evidence for an impact origin of pallasites. *Earth and Planetary Science Letters*, 584:117440, Apr. 2022. doi: 10.1016/j.epsl.2022.117440. URL `https://doi.org/10.1016/j.epsl.2022.117440`.

S. K. Lam, A. Pitrou, and S. Seibert. Numba: A llvm-based python jit compiler. In *Proceedings of the Second Workshop on the LLVM Compiler Infrastructure in HPC*, pages 1–6, 2015.

H. P. Langtangen and S. Linge. *Finite Difference Computing with PDEs*. Springer International Publishing, 2017. doi: 10.1007/978-3-319-55456-3. URL `https://doi.org/10.1007/978-3-319-55456-3`.

S. J. McKibbin, L. Pittarello, C. Makarona, C. Hamann, L. Hecht, S. M. Chernonozhkin, S. Goderis, and P. Claeys. Petrogenesis of main group pallasite meteorites based on relationships among texture, mineralogy, and geochemistry. *Meteoritics & Planetary Science*, 54(11):2814–2844, 2019. doi: 10.1111/maps.13392. URL `https://onlinelibrary.wiley.com/doi/abs/10.1111/maps.13392`.

W. McKinney. Data Structures for Statistical Computing in Python. In Stéfan van der Walt and Jarrod Millman, editors, *Proceedings of the 9th Python in Science Conference*, pages 56 – 61, 2010. doi: 10.25080/Majora-92bf1922-00a.

M. Miyamoto. Chemical zoning of olivine in several pallasites. *Journal of Geophysical Research: Planets*, 102(E9):21613–21618, 1997. doi: 10.1029/97JE01852.

A. Morbidelli, K. Baillié, K. Batygin, S. Charnoz, T. Guillot, D. C. Rubie, and T. Kleine. Contemporary formation of early solar system planetesimals at two distinct radial locations. *Nature Astronomy*, 6(1): 72–79, 2022. doi: 10.1038/s41550-021-01517-7.

D. Mottaghy and V. Rath. Latent heat effects in subsurface heat transport modelling and their impact on palaeotemperature reconstructions. *Geophysical Journal International*, 164(1):236–245, 2006. doi: 10.1111/j.1365-246x.2005.02843.x.

M. Murphy Quinlan. PytesiMINT software package: v0.1.0. 2023. doi: 10.5281/zenodo.7907531.

M. Murphy Quinlan, A. M. Walker, C. J. Davies, J. E. Mound, T. Müller, and J. Harvey. The Conductive Cooling of Planetesimals With Temperature-Dependent Properties. *Journal of Geophysical Research: Planets*, 126(4), 2021a. doi: 10.1029/2020JE006726.

M. Murphy Quinlan, A. M. Walker, P. Selves, and L. S. E. Teggin. Pytesimal software package: v2.0.0. 2021b. doi: 10.5281/zenodo.4762445.

C. I. O. Nichols, J. F. J. Bryson, R. D. Cottrell, R. R. Fu, R. J. Harrison, J. Herrero-Albillos, F. Kronast, J. A. Tarduno, and B. P. Weiss. A Time-Resolved Paleomagnetic Record of Main Group Pallasites: Evidence for a Large-Cored, Thin-Mantled Parent Body. *Journal of Geophysical Research: Planets*, 126 (7):e2021JE006900, 2021. doi: https://doi.org/10.1029/2021JE006900.

M. Özısık. *Heat conduction*. Wiley, New York, 1993.

K. Saiki, D. Laporte, D. Vielzeuf, S. Nakashima, and P. Boivin. Morphological analysis of olivine grains annealed in an iron-nickel matrix: Experimental constraints on the origin of pallasites and on the thermal history of their parent bodies. *Meteoritics & Planetary Science*, 38(3):427–444, 2003.

E. R. Scott. Formation of olivine-metal textures in pallasite meteorites. *Geochimica et Cosmochimica Acta*, 41(6):693–710, jun 1977. doi: 10.1016/0016-7037(77)90043-6. URL `https://doi.org/10.1016/0016-7037(77)90043-6`.

E. R. D. Scott. Pallasites: Olivine-metal textures, metal compositions, minor phases, origins, and insights into processes at core-mantle boundaries of asteroids. In *Lunar and Planetary Science XLVIII*, page 1037 (abstr.), Lunar Planet. Inst., Houston., 2017.

G. F. Solferino and G. J. Golabek. Olivine grain growth in partially molten Fe–Ni–S: A proxy for the genesis of pallasite meteorites. *Earth and Planetary Science Letters*, 504:38–52, 2018. Publisher: Elsevier.

G. F. Solferino, G. J. Golabek, F. Nimmo, and M. W. Schmidt. Fast grain growth of olivine in liquid Fe–S and the formation of pallasites with rounded olivine grains . *Geochimica et Cosmochimica Acta*, 162:259–275, aug 2015. doi: 10.1016/j.gca.2015.04.020. URL `https://doi.org/10.1016/j.gca.2015.04.020`.

G. F. D. Solferino, P.-R. Thomson, and S. Hier-Majumder. Pore network modeling of core forming melts in planetesimals. *Frontiers in Earth Science*, 8:339, Aug 2020. doi: 10.3389/feart.2020.00339. URL `https://www.frontiersin.org/article/10.3389/feart.2020.00339/full`.

T. Stephens, R. Walker, D. Healy, and A. Bubeck. Segment tip geometry of sheet intrusions, ii: Field observations of tip geometries and a model for evolving emplacement mechanisms. *Volcanica*, 4(2):203–225, Oct 2021. doi: 10.30909/vol.04.02.203225. URL `https://www.jvolcanica.org/ojs/index.php/volcanica/article/view/109`.

J. A. Tarduno, R. D. Cottrell, F. Nimmo, J. Hopkins, J. Voronov, A. Erickson, E. Blackman, E. R. Scott, and R. McKinley. Evidence for a dynamo in the main group pallasite parent body. *Science*, 338(6109):939–942, 2012. doi: 10.1126/science.1223932. URL `https://www.science.org/doi/abs/10.1126/science.1223932`.

T. Tomiyama and G. R. Huss. Minor and trace element zoning in pallasite olivine: modeling pallasite thermal history. *Lunar Planet.Sci.*, 37:2132, 2006. URL `www.scopus.com`. Cited By :3.

P. Virtanen, R. Gommers, T. E. Oliphant, M. Haberland, T. Reddy, D. Cournapeau, E. Burovski, P. Peterson, W. Weckesser, J. Bright, S. J. van der Walt, M. Brett, J. Wilson, K. J. Millman, N. Mayorov, A. R. J. Nelson, E. Jones, R. Kern, E. Larson, C. J. Carey, İ. Polat, Y. Feng, E. W. Moore, J. VanderPlas, D. Laxalde, J. Perktold, R. Cimrman, I. Henriksen, E. A. Quintero, C. R. Harris, A. M. Archibald, A. H. Ribeiro, F. Pedregosa, P. van Mulbregt, and SciPy 1.0 Contributors. SciPy 1.0: Fundamental Algorithms for Scientific Computing in Python. *Nature Methods*, 17:261–272, 2020. doi: 10.1038/s41592-019-0686-2.

R. Walker, T. Stephens, C. Greenfield, S. Gill, D. Healy, and S. Poppe. Segment tip geometry of sheet intrusions, i: Theory and numerical models for the role of tip shape in controlling propagation pathways. *Volcanica*, 4(2):189–201, Oct 2021. doi: 10.30909/vol.04.02.189201. URL `https://www.jvolcanica.org/ojs/index.php/volcanica/article/view/114`.

N. P. Walte and G. J. Golabek. Olivine aggregates reveal a complex collisional history of the main group pallasite parent body. *Meteoritics & Planetary Science*, 57(5):1098–1115, 2022. doi: 10.1111/maps.13810. URL `https://onlinelibrary.wiley.com/doi/abs/10.1111/maps.13810`.

N. P. Walte, G. F. D. Solferino, G. J. Golabek, D. Silva Souza, and A. Bouvier. Two-stage formation of pallasites and the evolution of their parent bodies revealed by deformation experiments. *Earth and Planetary Science Letters*, 546:116419, 2020. ISSN 0012-821X. doi: 10.1016/j.epsl.2020.116419.

R. J. Windmill, I. A. Franchi, J. L. Hellmann, J. M. Schneider, F. Spitzer, T. Kleine, R. C. Greenwood, and M. Anand. Isotopic evidence for pallasite formation by impact mixing of olivine and metal during the first 10 million years of the solar system. *PNAS Nexus*, 1(1), Mar. 2022. doi: 10.1093/pnasnexus/pgac015. URL `https://doi.org/10.1093/pnasnexus/pgac015`.

N. N. Yanenko. *The Method of Fractional Steps*. Springer Berlin Heidelberg, 1971. doi: 10.1007/978-3-642-65108-3.

C. W. Yang, D. B. Williams, and J. I. Goldstein. A new empirical cooling rate indicator for meteorites based on the size of the cloudy zone of the metallic phases. *Meteoritics & Planetary Science*, 32(3):423–429, 1997.

J. Yang, J. I. Goldstein, and E. R. Scott. Main-group pallasites: Thermal history, relationship to IIIAB irons, and origin. *Geochimica et Cosmochimica Acta*, 74(15):4471–4492, 2010. ISSN 0016-7037. doi: 10.1016/j.gca.2010.04.016.

M. Zeneli, A. Nikolopoulos, S. Karellas, and N. Nikolopoulos. Numerical methods for solid-liquid phase-change problems. In *Ultra-High Temperature Thermal Energy Storage, Transfer and Conversion*, pages 165–199. Elsevier, 2021. doi: 10.1016/b978-0-12-819955-8.00007-7.

Supplementary materials for: Reconciling fast and slow cooling during planetary formation as recorded in the main group pallasites

M. Murphy Quinlan*[1] A. M. Walker[2] C. J. Davies[1]

*Email: eememq@leeds.ac.uk
[1]*School of Earth and Environment, University of Leeds, Leeds, UK*
[2]*Department of Earth Sciences, University of Oxford, Oxford, UK*

1 Extended methods

Our intrusion model consists of an ellipsoid region of interconnected solid olivine bridgework (Boesenberg et al., 2012), the pore space (created by inter- and intra-granular fractures) of which has been infiltrated and saturated by initially molten metal. This intrusion region is surrounded by a portion of the planetesimal mantle. We assume convection of the metal in this region is inhibited by the low porosity and permeability of the solid olivine bridgework, the rapid crystallisation of the metal, and the low gravitational acceleration.

We consider a cartesian box of mantle material with constant temperature in the horizontal directions x and y, and the vertical coordinate z aligned with the 1D mantle temperature output from the planetesimal model. Assuming a purely conductive system in which convective heat transport and internal heat generation are neglected, the temperature T (K) in this volume satisfies the three-dimensional heat conduction equation (Carslaw and Jaeger, 1959):

$$\rho c_p \frac{\partial T}{\partial t} = \frac{\partial}{\partial x}\left(k\frac{\partial T}{\partial x}\right) + \frac{\partial}{\partial y}\left(k\frac{\partial T}{\partial y}\right) + \frac{\partial}{\partial z}\left(k\frac{\partial T}{\partial z}\right) \tag{1}$$

where: ρ is the density of the material ($\mathrm{kg\,m^{-3}}$); c_p is the specific heat capacity ($\mathrm{J\,kg^{-1}\,K^{-1}}$); t is time (s); x, y, and z are the spatial coordinates (m); and k is thermal conductivity ($\mathrm{W\,m^{-1}\,K^{-1}}$). We choose temperature-independent k, allowing the Crank-Nicolson scheme to be applied to the problem without the complications associated with non-linearity (Carslaw and Jaeger, 1959; Özısık, 1993).

We define a uniaxial ellipsoid centered in the box, of volume $V = \frac{4}{3}\pi a^2 b$, where a and b are radii, which represents the intrusion region with a pallasitic mix of silicate and metal. The dimensions of the box ($X = Y = Z$) enclosing this ellipsoid is set by the diffusion lengthscale for the mantle material: we wish to run the model for ten years, and do not want the temperature near the model boundaries to change during that time. This allows us to apply a zero-flux condition to the boundaries of the problem.

Directly modelling the mixed-phase region of olivine crystals and metal melt would be computationally expensive and require detailed knowledge of the geometry of the phase mixture. Instead, we take a macroscopic approach to track the cooling and crystallisation of the metal in this area, and consider the intrusion region as a homogeneous, isotropic material, using volume-averaged effective thermal properties. We adopt the method of Mottaghy and Rath (2006) to model permafrost: we assume a simple saturated two component system, where olivine forms a solid interconnected bridgework of crystals, with the pore space filled with metal.

The volume fraction of metal-saturated pore space is denoted by ϕ_m, while the olivine fraction is labelled ϕ_{ol}, with $\phi_{ol} + \phi_m = 1$. We can then replace ρc_p in equation 1 with the arithmetic mean of ρc_p for metal and olivine ($\rho_m c_m$ and $\rho_{ol} c_{ol}$), and k with the square-root mean for both phases (k_m and k_{ol}) as this is more physically realistic for a randomly distributed mixture (Mottaghy and Rath, 2006; Roy et al., 1981):

$$\rho c_p = \phi_m \rho_m \, c_m + \phi_{ol} \rho_{ol} \, c_{ol} \,, \quad k = \left(\phi_m \sqrt{k_m} + \phi_{ol} \sqrt{k_{ol}}\right)^2 . \tag{2}$$

The metal-filled porosity can be further divided into the solid ($\phi_{m(s)}$) and liquid ($\phi_{m(l)}$) fractions:

$$\phi_m = \phi_{m(s)} + \phi_{m(l)}. \tag{3}$$

The fraction of solid and liquid metal is controlled by a temperature-dependent function which should be one when the metal is entirely solid ($T < T_S$, the solidus temperature), and zero when the metal is fluid ($T > T_L$, the liquidus temperature). We use the differentiable equation suggested by Mottaghy and Rath (2006):

$$\Theta = \begin{cases} \exp\left[-\left(\frac{T-T_\mathrm{L}}{w}\right)^2\right] & \text{if} \quad T < T_\mathrm{L}, \\ 1 & \text{if} \quad T > T_\mathrm{L}, \end{cases} \tag{4}$$

where w is just $\frac{\Delta T}{2} = \frac{T_L - T_S}{2}$. This is differentiable:

$$\frac{d\Theta}{dT} = \begin{cases} -\frac{2(T-T_\mathrm{L})}{w^2}\exp\left[-\left(\frac{T-T_\mathrm{L}}{w}\right)^2\right] & \text{if} \quad T \leq T_\mathrm{L}, \\ 0 & \text{if} \quad T > T_\mathrm{L}. \end{cases} \tag{5}$$

We apply this to the crystallisation of meteoritic Fe-Ni-S metal (Fig. S1), with $T_L = 1600$ K and $T_S = 1260$ K (Wasson and Choi, 2003, Ehlers, 1972).

To account for the latent heat associated with melting or crystallisation, we apply the simple fixed-domain apparent heat capacity method which correlates the heat capacity of the phase-changing material with the slope of the enthalpy-temperature curve (Zeneli et al., 2021). We add a term to the heat capacity of the component that experiences the phase change—in this case, the metal—to define a new apparent volumetric heat capacity ($\rho c_{m,app}$; Sarbu and Sebarchievici, 2017):

$$\phi_m \rho c_{m,app} = \phi_{m(l)}\,\rho_{m(l)}\,c_{m(l)} + \phi_{m(s)}\,\rho_{m(s)}\,c_{m(s)} + \rho_{m(l)}\,L\,\frac{\partial \phi_{m(l)}}{\partial T}, \tag{6}$$

where L is the specific latent heat of fusion (J kg^{-1}). This can then be substituted in to equation 2 to find the overall apparent heat capacity of the mixed region; similarly, the conductivity can be modified to accommodate the solid and liquid metal phase. Diffusivity (κ, m^2 s^{-1}) can be defined for all the phases in the mixed region, including the phase change effects:

$$\kappa = \frac{k}{\rho c_p} = \frac{\left(\phi_{m(l)}\sqrt{k_{m(l)}} + \phi_{m(s)}\sqrt{k_{m(s)}} + \phi_{ol}\sqrt{k_{ol}}\right)^2}{\phi_{m(l)}\rho_{m(l)}c_{m(l)} + \phi_{m(s)}\rho_{m(s)}c_{m(s)} + \rho_{m(l)}L\,\frac{\partial \phi_{m(l)}}{\partial T} + \phi_{ol}\rho_{ol}\,c_{ol}}. \tag{7}$$

While diffusivity inside the ellipsoidal intrusion region is defined by equation 7, the material properties outside the intrusion have either constant values that match that of olivine, or use the same equations but with a smaller fraction of metal (to approximate metal trapped in the mantle). Sudden jumps and step functions in the spatially-varying diffusivity can introduce instabilities especially if these material properties boundaries intersect with the model boundary. We ensure this does not happening by centering our intrusion ellipsoid within mantle material with spatially-constant material properties, so that the model boundary never crosses the mantle-intrusion boundary.

1.1 Numerical approach

To illustrate our approach, we first consider the heat equation in 1D and write it in terms of spatially varying diffusivity:

$$\frac{\partial T}{\partial t} = \frac{\partial}{\partial x}\left(\kappa(x)\frac{\partial T}{\partial x}\right) + \text{I.B.C.}, \tag{8}$$

where I.B.C. stands for initial and boundary conditions. We apply the semi-implicit Crank-Nicolson scheme (Crank and Nicolson, 1947) with zero-flux boundary conditions. Forward difference is used for the time derivative of T, and the spatial derivative is evaluated at the time step $n + 1/2$ instead of at n, taking the arithmetic mean between the time step n and $n + 1$. We also discretise κ with respect to distance, i, using finite differences (Langtangen and Linge, 2017).

After expansion and simplification, the resulting system of linear equations can be represented in matrix form: $A\mathbf{T}^{n+1} + \mathbf{b}^{n+1} = B\mathbf{T}^{n} + \mathbf{b}^{n}$, where A and B are $N \times N$ matrices, $\mathbf{T}^{n+1}$ and $\mathbf{T}^{n}$ are column vectors of temperature at times $n+1$ and n, and $\mathbf{b}^{n}$ and $\mathbf{b}^{n+1}$ are boundary condition column vectors. For zero-flux boundary conditions, these column vectors are zero. We define a new parameter in place of the Fourier number, with variable diffusivity: $\mathbf{r}_i = \kappa_i \Delta t / \Delta x^2$, where Δt is the time step and Δx is the spatial step. We can then define the upper, lower and diagonal coefficients of A and B:

$$\begin{aligned} R_i^U &= r_i + r_{i+1}, \\ R_i^L &= r_i + r_{i-1}, \\ R_i^D &= 2r_i + r_{i+1} + r_{i-1}. \end{aligned} \tag{9}$$

The matrix equation can then be written:

$$\begin{aligned} &\begin{pmatrix} 4+R_0^D & -2R_0^U & & & \\ -R_1^L & 4+R_1^D & -r_1 & 0 & \\ & & \ddots & & \\ & 0 & -R_{N-1}^L & 4+R_{N-1}^D & -R_{N-1}^U \\ & & & -2R_N^L & 4+R_N^D \end{pmatrix} \begin{pmatrix} T_0^{n+1} \\ T_1^{n+1} \\ \vdots \\ T_{N-1}^{n+1} \\ T_N^{n+1} \end{pmatrix} \\ = &\begin{pmatrix} 4-R_0^D & 2R_0^U & & & \\ R_1^L & 4-R_1^D & R_1^U & 0 & \\ & & \ddots & & \\ & 0 & R_{N-1}^L & 4-R_{N-1}^D & R_{N-1}^U \\ & & & 2R_N^L & 4-R_N^D \end{pmatrix} \begin{pmatrix} T_0^{n} \\ T_1^{n} \\ \vdots \\ T_{N-1}^{n} \\ T_N^{n} \end{pmatrix}. \end{aligned} \tag{10}$$

This requires that $\mathbf{r}$ is a column vector with two ghost points at r_{-1} and r_{N+1}. In order to find the temperature distribution at the next time step, we multiply across by the inverse of A: $\mathbf{T}_i^{n+1} = \left(A^{-1}B\right)\mathbf{T}_i^{n}$. The full derivation of these matrix equations can be found in the supplementary information.

In order to extend this scheme to three dimensions, we apply the Fractional Step Method (Cen et al., 2016; Yanenko, 1971), which evaluates the heat equation in one-third time step increments along each of the spatial dimensions i, j and k:

$$\begin{aligned} A\mathbf{T}_{j,k}^{n+\frac{1}{3}} &= B\mathbf{T}_{j,k}^{n}, \\ A\mathbf{T}_{i,k}^{n+\frac{2}{3}} &= B\mathbf{T}_{i,k}^{n+\frac{1}{3}}, \\ A\mathbf{T}_{i,j}^{n+1} &= B\mathbf{T}_{i,j}^{n+\frac{2}{3}}, \end{aligned} \tag{11}$$

where the superscript $\left(n+\frac{1}{3}\right)$ refers to the fractional time step $t^{n+\frac{1}{3}} = t^n + \frac{1}{3}\Delta t$ and so on. The temperature distribution at the next time step is found by evaluating these three one-dimensional equations in turn instead of one three-dimensional equation (Sahijpal, 2021).

We bench-marked our numerical model against an analytical solution from Carslaw and Jaeger (1959), and found that the maximum relative defect between the numerical and analytical models dropped to below 1 % within 150 seconds (Figure S2).

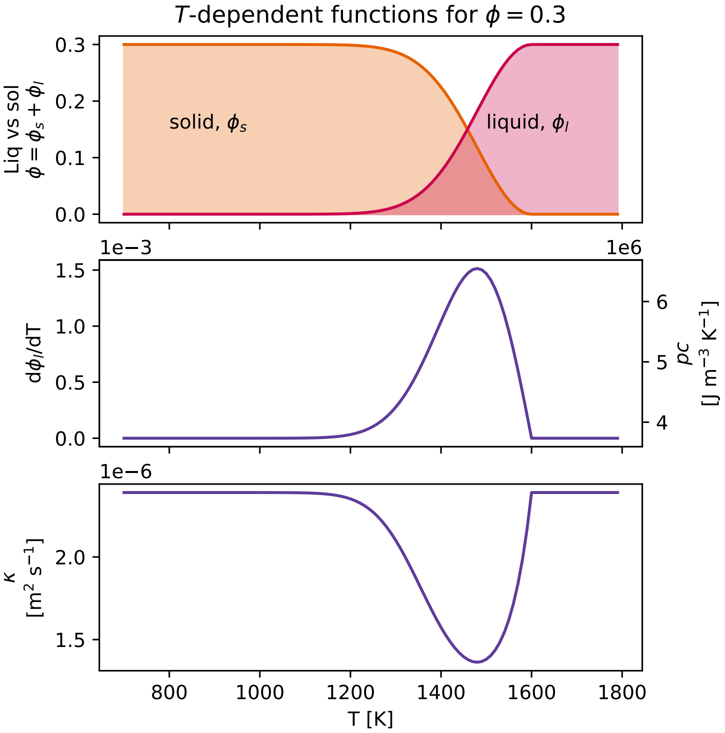

Figure S1: Temperature dependent functions for a mixed region of 30 % phase-change material (PCM - in this case, metal - ϕ), and 70 % non-PCM, in this case olivine $(1-\phi)$. The functions for κ and ρc are for this mixture. To simplify the problem, we have set the material properties for liquid and solid metal as equal; however, the code allows these to be varied independently.

2 Additional figures relating to benchmarking and sensitivity analyses

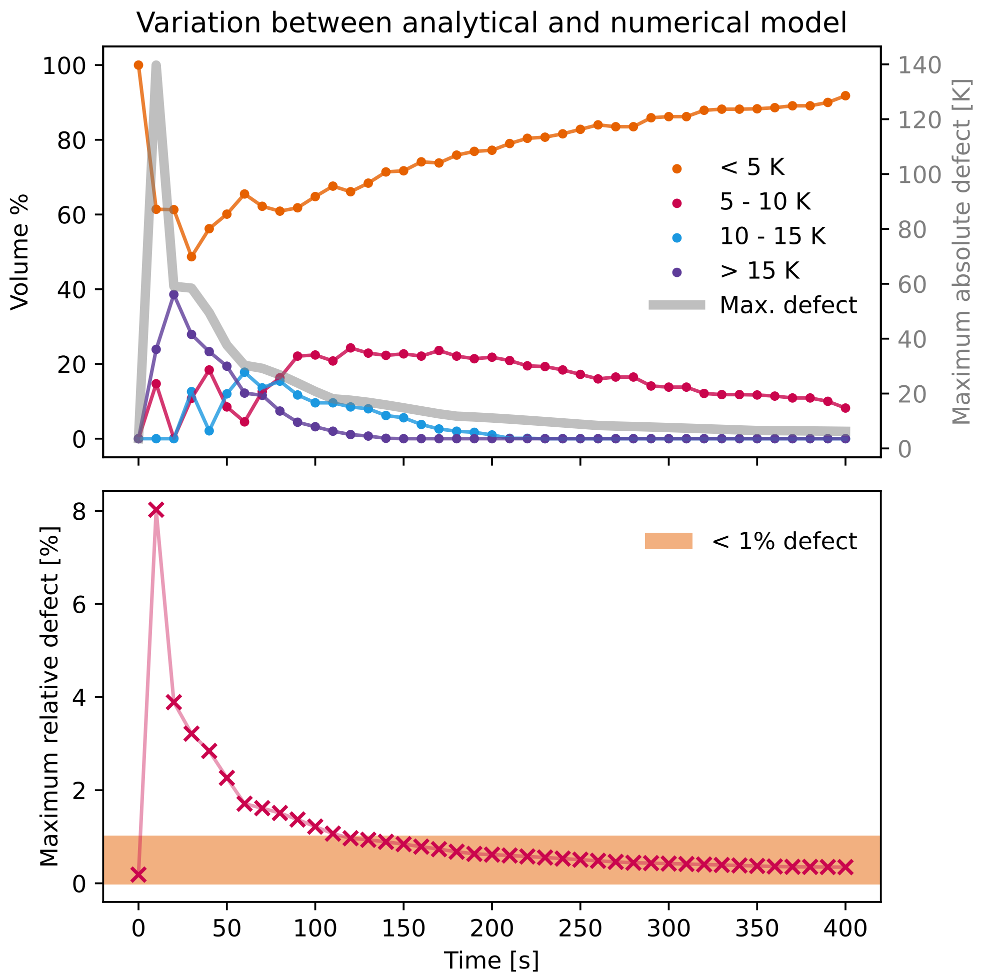

Figure S2: The numerical model was set up to closely approximate a cube with fixed-temperature boundary conditions and spatially constant diffusivity, and the results were compared to the output of an analytical solution for the same geometry (Carslaw and Jaeger, 1959). Within 150 seconds, the maximum relative defect drops below 1 %, with the majority of the numerically modelled region within 5 K of the analytical solution (comparing voxel to equivalent voxel).

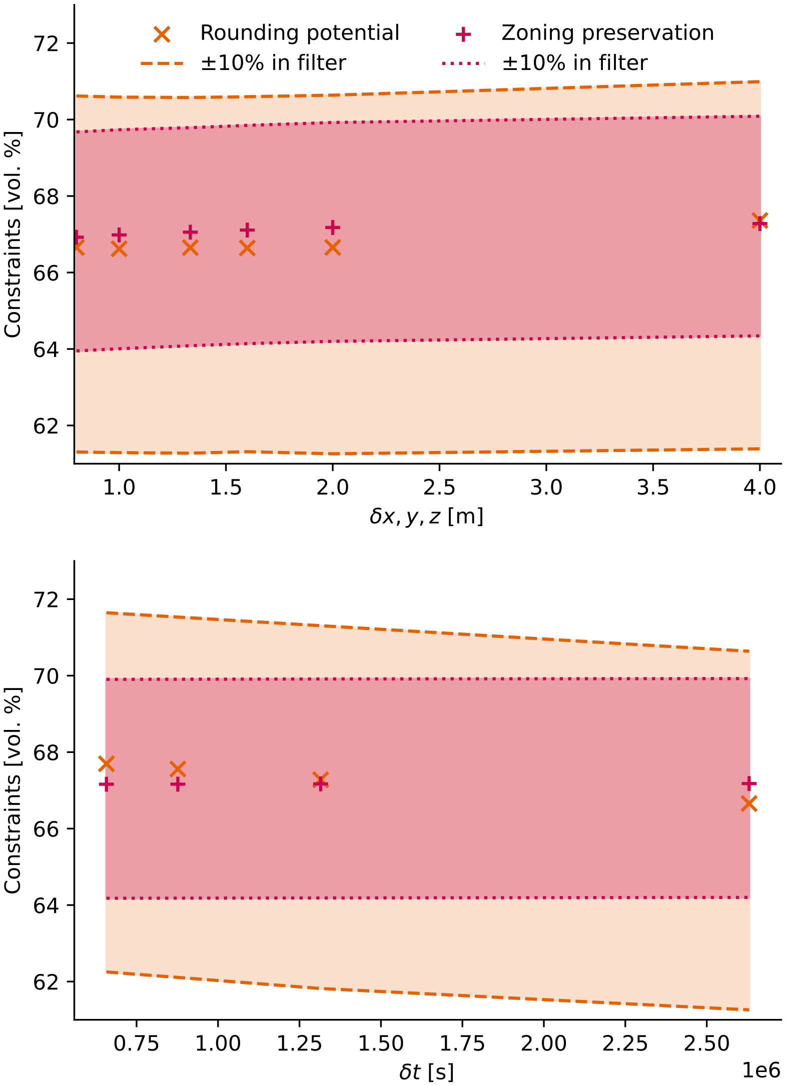

Figure S3: Exploration of effect of model resolution and rounding potential/zoning preservation. Spatial step size of < 4 m or time step $< 2.63 \times 10^6$ s (~ 1 month) results in a change in either result by < 1 %. These are compared to the effect of increasing or decreasing the temperature cutoffs for the rounding and zoning criteria.

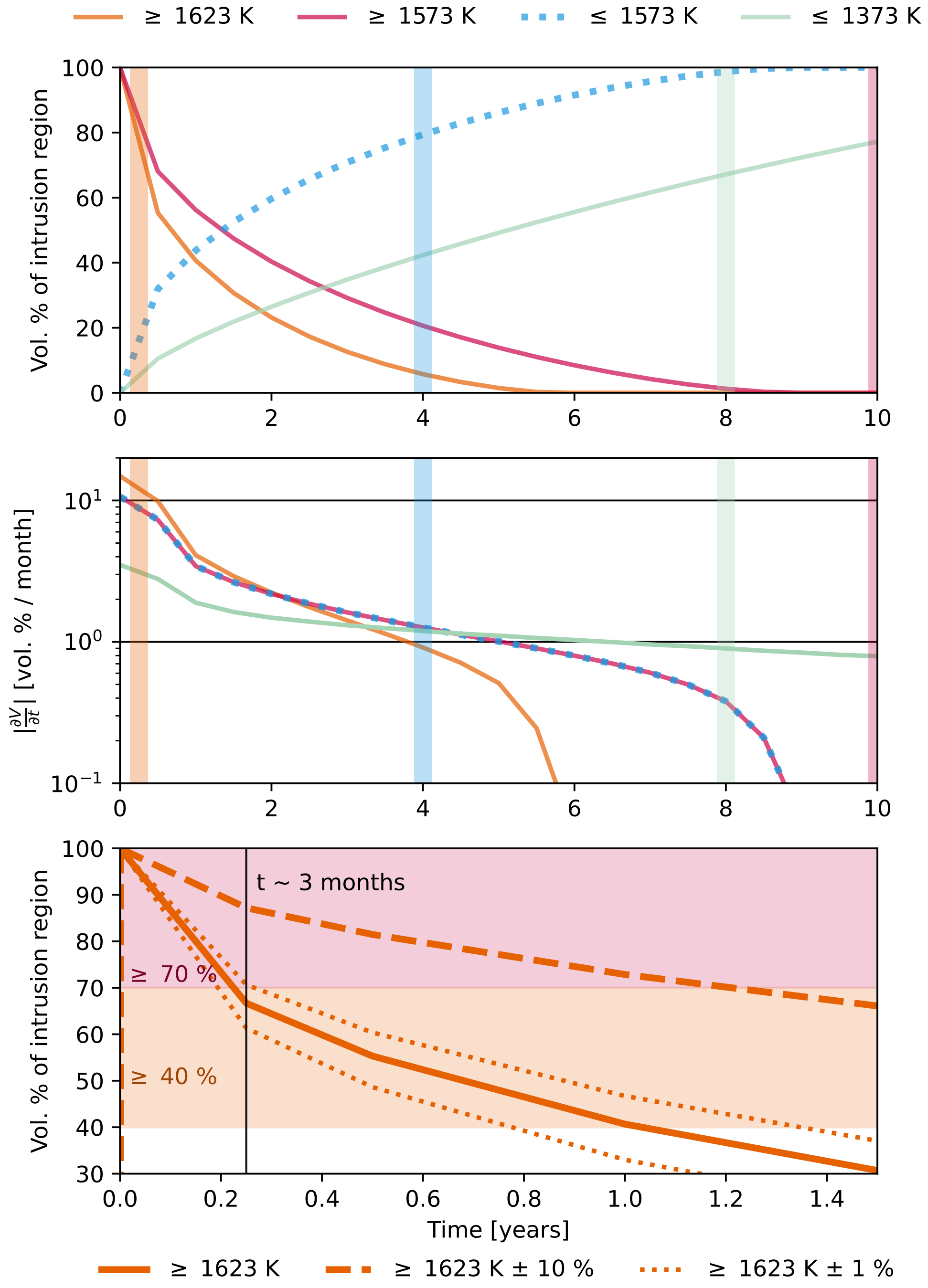

Figure S4: Exploration of the effect of time of measurement for each of the rounding and zoning criteria. The top panel shows the volume % of the region of the intrusion that matches each requirement through time, and the corresponding time that this measurement is taken (matching colour vertical line). The second panel shows the rate of change of intrusion volume that matches each criterion, per month (where the timestep is $\sim$ 1 month). The botom panel is a zoomed view of the first criteria ($T_{\text{3mnths}} \geq 1623$ K), which is the most sensitive to timing. This plot also shows the volume % of the region that matches the criteria if the temperature requirement is varied by ± 10 % or ± 1 %. The rounding requirement volume is shown in shaded orange, with an additional ± 5 % shown in pink.

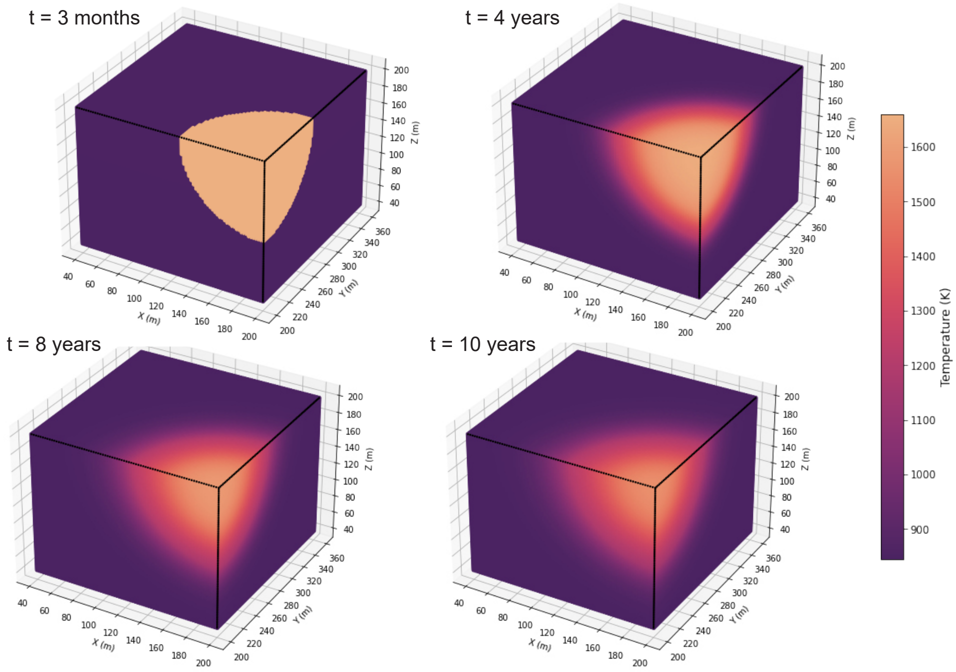

Figure S5: 3D heat-map of the example case illustrated in the main text, taken at times when rounding and zoning criteria are measured. This shows a quarter of the total intrusion volume, centred on the intrusion.

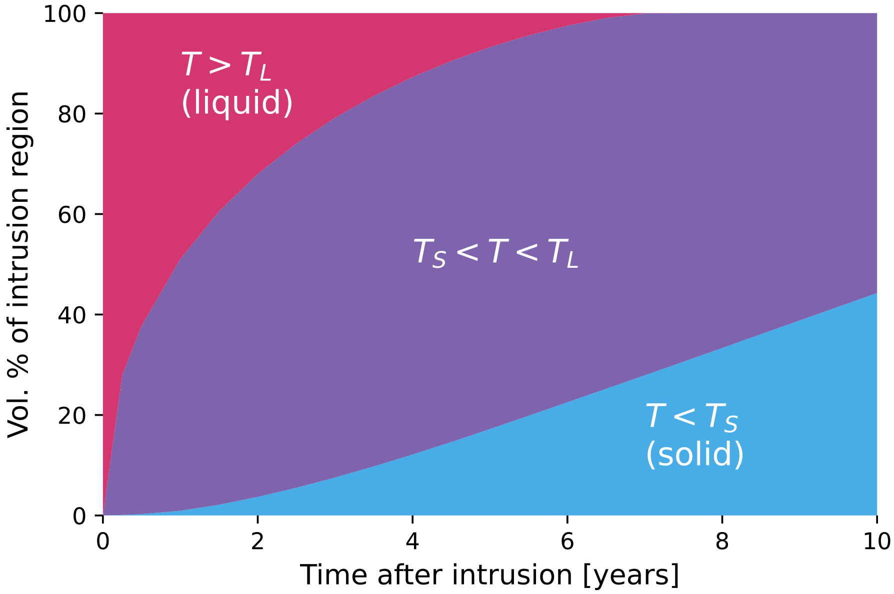

Figure S6: Volume % of the intrusion region above and below metal solidus and liquidus temperatures, where T_L is liquidus temperature, T_S is solidus temperature, and T is the temperature of a voxel of the intrusion region for the example case illustrated in the main text.

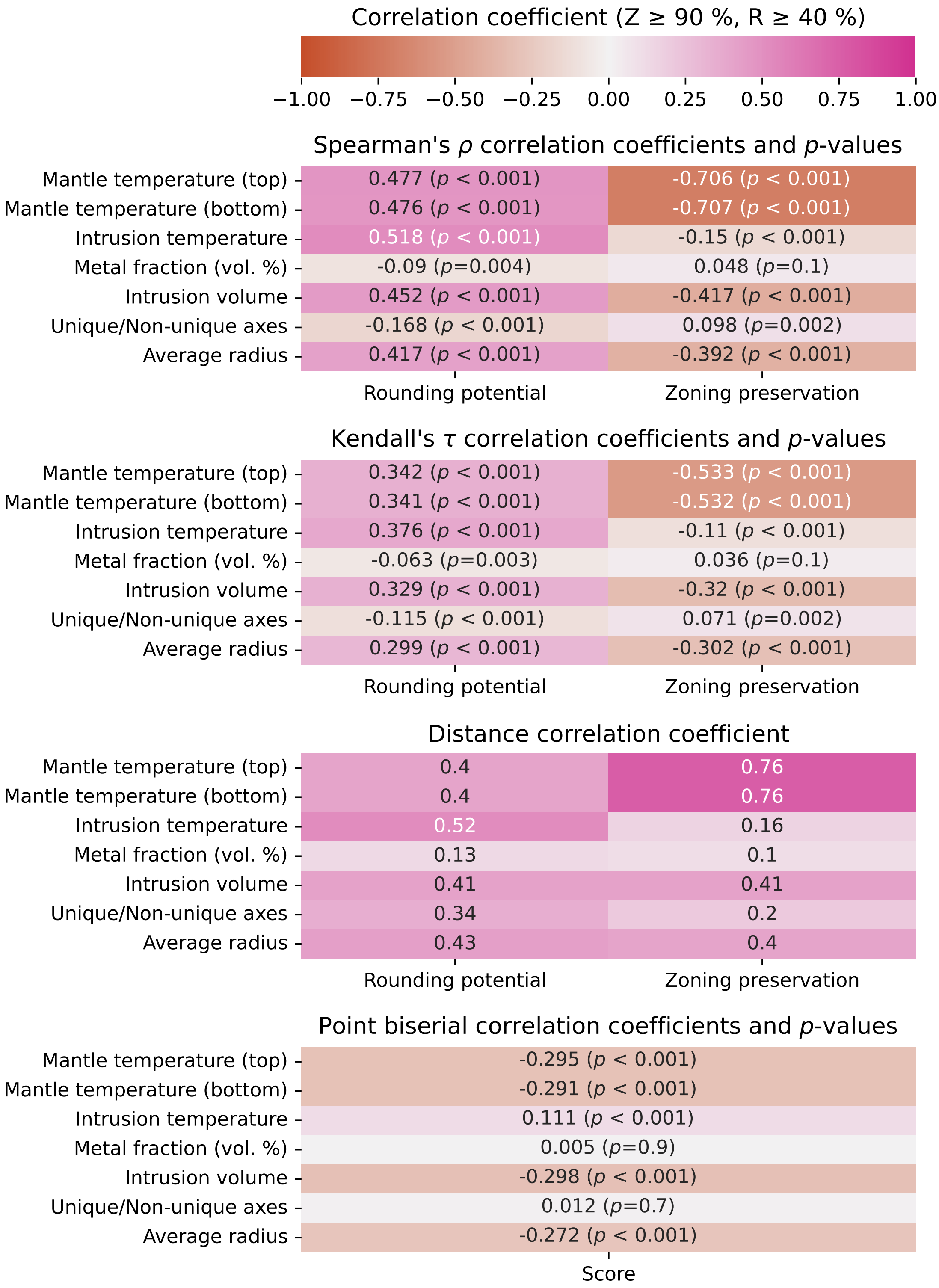

Spearman's ρ correlation coefficients and p-values

	Rounding potential	Zoning preservation
Mantle temperature (top)	0.477 ($p < 0.001$)	-0.706 ($p < 0.001$)
Mantle temperature (bottom)	0.476 ($p < 0.001$)	-0.707 ($p < 0.001$)
Intrusion temperature	0.518 ($p < 0.001$)	-0.15 ($p < 0.001$)
Metal fraction (vol. %)	-0.09 (p=0.004)	0.048 (p=0.1)
Intrusion volume	0.452 ($p < 0.001$)	-0.417 ($p < 0.001$)
Unique/Non-unique axes	-0.168 ($p < 0.001$)	0.098 (p=0.002)
Average radius	0.417 ($p < 0.001$)	-0.392 ($p < 0.001$)

Kendall's τ correlation coefficients and p-values

	Rounding potential	Zoning preservation
Mantle temperature (top)	0.342 ($p < 0.001$)	-0.533 ($p < 0.001$)
Mantle temperature (bottom)	0.341 ($p < 0.001$)	-0.532 ($p < 0.001$)
Intrusion temperature	0.376 ($p < 0.001$)	-0.11 ($p < 0.001$)
Metal fraction (vol. %)	-0.063 (p=0.003)	0.036 (p=0.1)
Intrusion volume	0.329 ($p < 0.001$)	-0.32 ($p < 0.001$)
Unique/Non-unique axes	-0.115 ($p < 0.001$)	0.071 (p=0.002)
Average radius	0.299 ($p < 0.001$)	-0.302 ($p < 0.001$)

Distance correlation coefficient

	Rounding potential	Zoning preservation
Mantle temperature (top)	0.4	0.76
Mantle temperature (bottom)	0.4	0.76
Intrusion temperature	0.52	0.16
Metal fraction (vol. %)	0.13	0.1
Intrusion volume	0.41	0.41
Unique/Non-unique axes	0.34	0.2
Average radius	0.43	0.4

Point biserial correlation coefficients and p-values

	Score
Mantle temperature (top)	-0.295 ($p < 0.001$)
Mantle temperature (bottom)	-0.291 ($p < 0.001$)
Intrusion temperature	0.111 ($p < 0.001$)
Metal fraction (vol. %)	0.005 (p=0.9)
Intrusion volume	-0.298 ($p < 0.001$)
Unique/Non-unique axes	0.012 (p=0.7)
Average radius	-0.272 ($p < 0.001$)

Figure S7: Monotonic and non-monotonic estimations of correlation with p value where relevant, for a suite of initial conditions and resulting volume % that match the rounding and zoning preservation criteria, as well as the overall score (where score was reduced to a binary pass/fail, with scores of 0 and 1 grouped into the fail category).

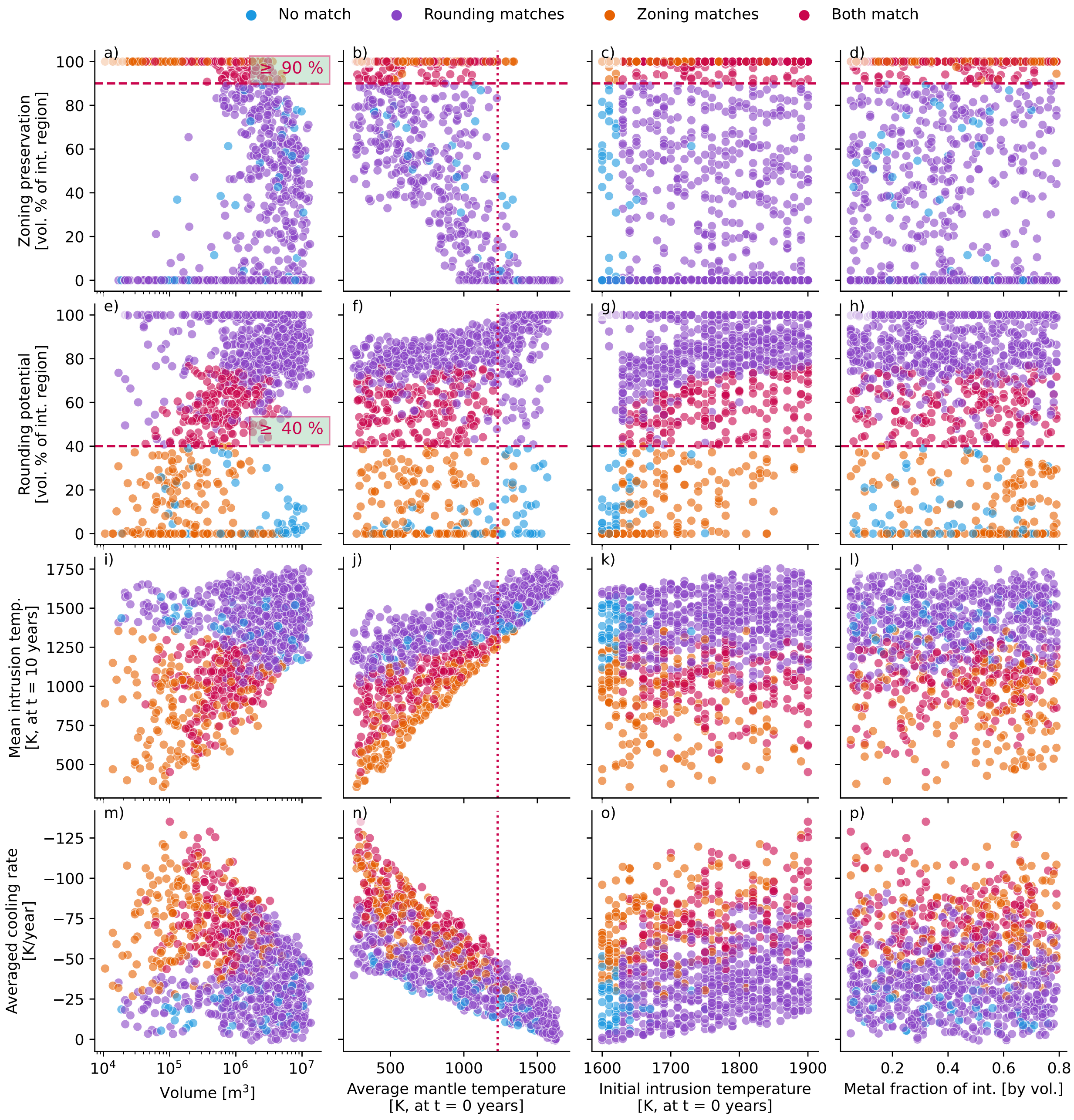

Figure S8: Summary of results for 1000 model runs (Z ≥ 90 %, R ≥ 40 %) where material properties were allowed to vary randomly in addition to geometry-related parameters. Vertical dotted line represents highest background mantle temperature where both criteria are met.

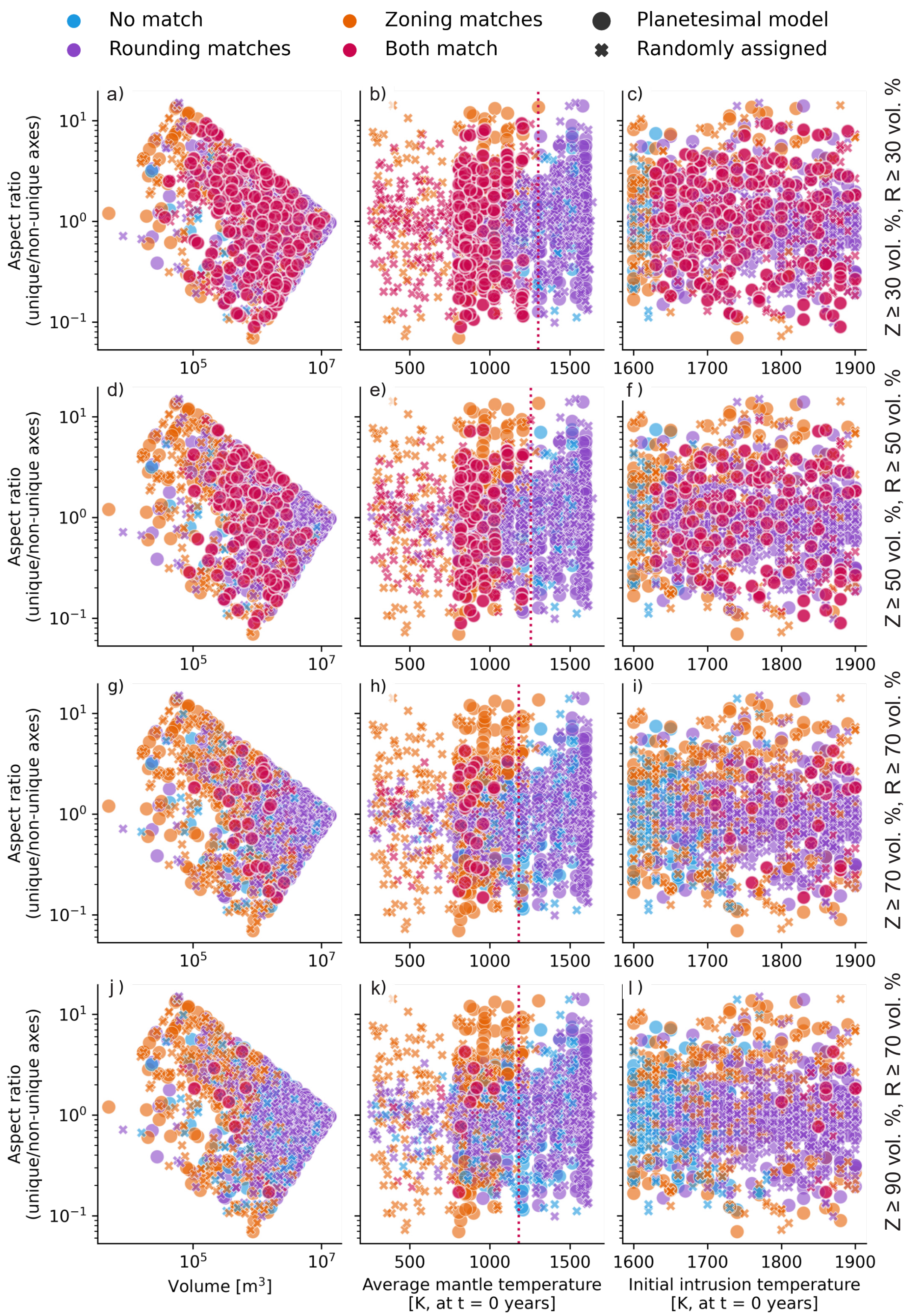

Figure S9: Summary of results for 1200 model runs with varying zoning and rounding criteria, showing that overall trends and conclusions stay the same. Colour denotes constraints matched, while marker shape describes the initial temperature conditions: either output from a planetesimal model, or randomly assigned. Parameters were not varied in isolation. Large pink circles match both constraints and used input from a planetesimal model.

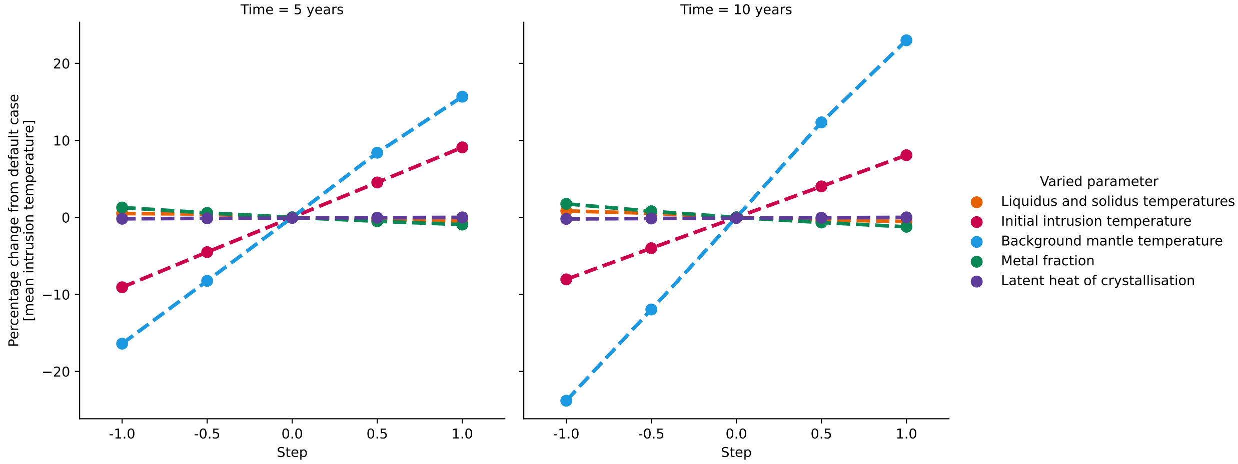

Figure S10: Sensitivity testing; varying parameters individually across a maximum, minimum and mean value. Details given in Table S1.

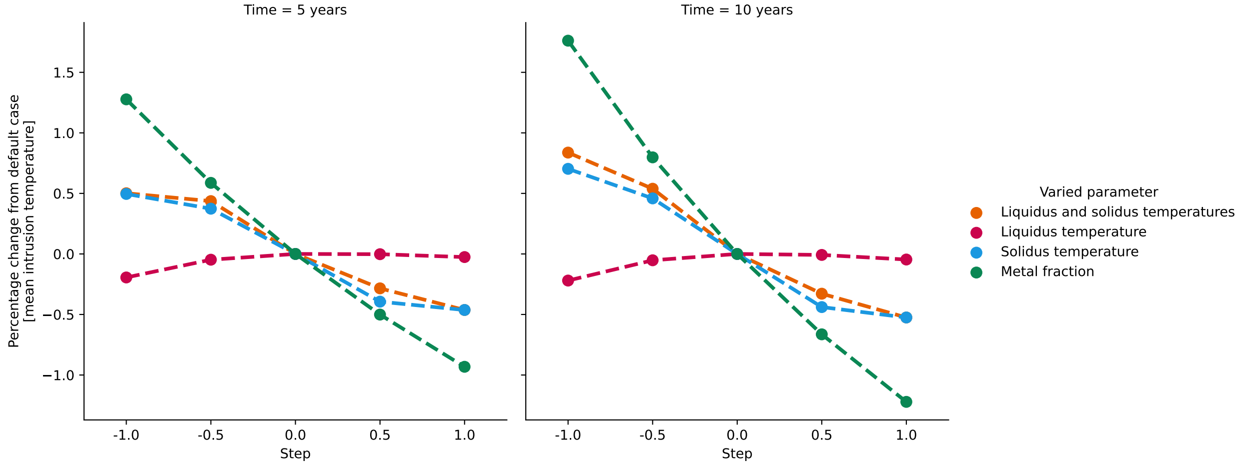

Figure S11: Sensitivity testing; varying parameters individually across a maximum, minimum and mean value, zoom in on less sensitive parameters. Details given in Table S1.

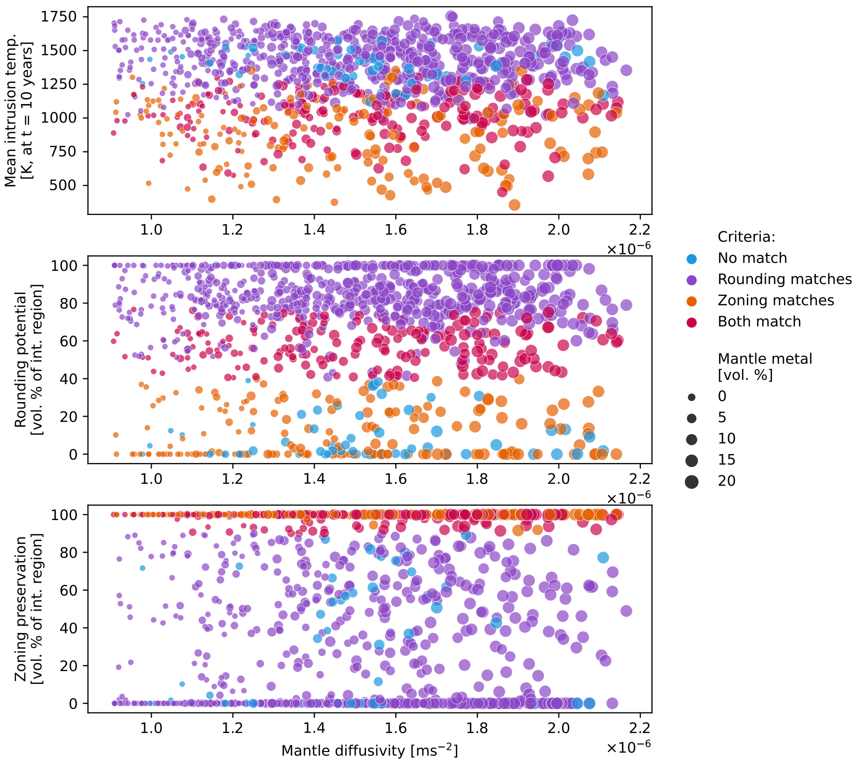

Figure S12: Summary of results for 1000 model runs ($Z \geq 90$ %, $R \geq 40$ %) where material properties were allowed to vary randomly in addition to geometry-related parameters, highlighting the effect of varying the proportion of trapped metal in the mantle and mantle diffusivity. Marker size denotes fraction of trapped metal in the planetesimal mantle. No significant correlation was found between fraction of metal trapped in the mantle and model score.

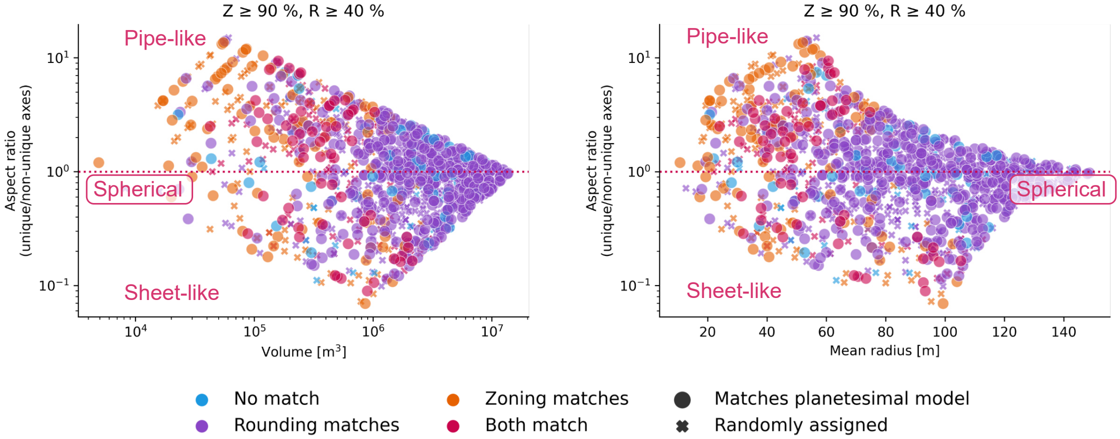

Figure S13: Exploration of intrusion region aspect ratio vs. volume ($Z \geq 90$ %, $R \geq 40$ %), showing the volume and mean radius ($\sim$ vol.$^{\frac{1}{3}}$) plotted against the aspect ratio (unique/non-unique axes of a uniaxial ellipsoid) which varies between ~ 0.1 (sheet-like geometry) and ~ 10 (pipe-like geometry).

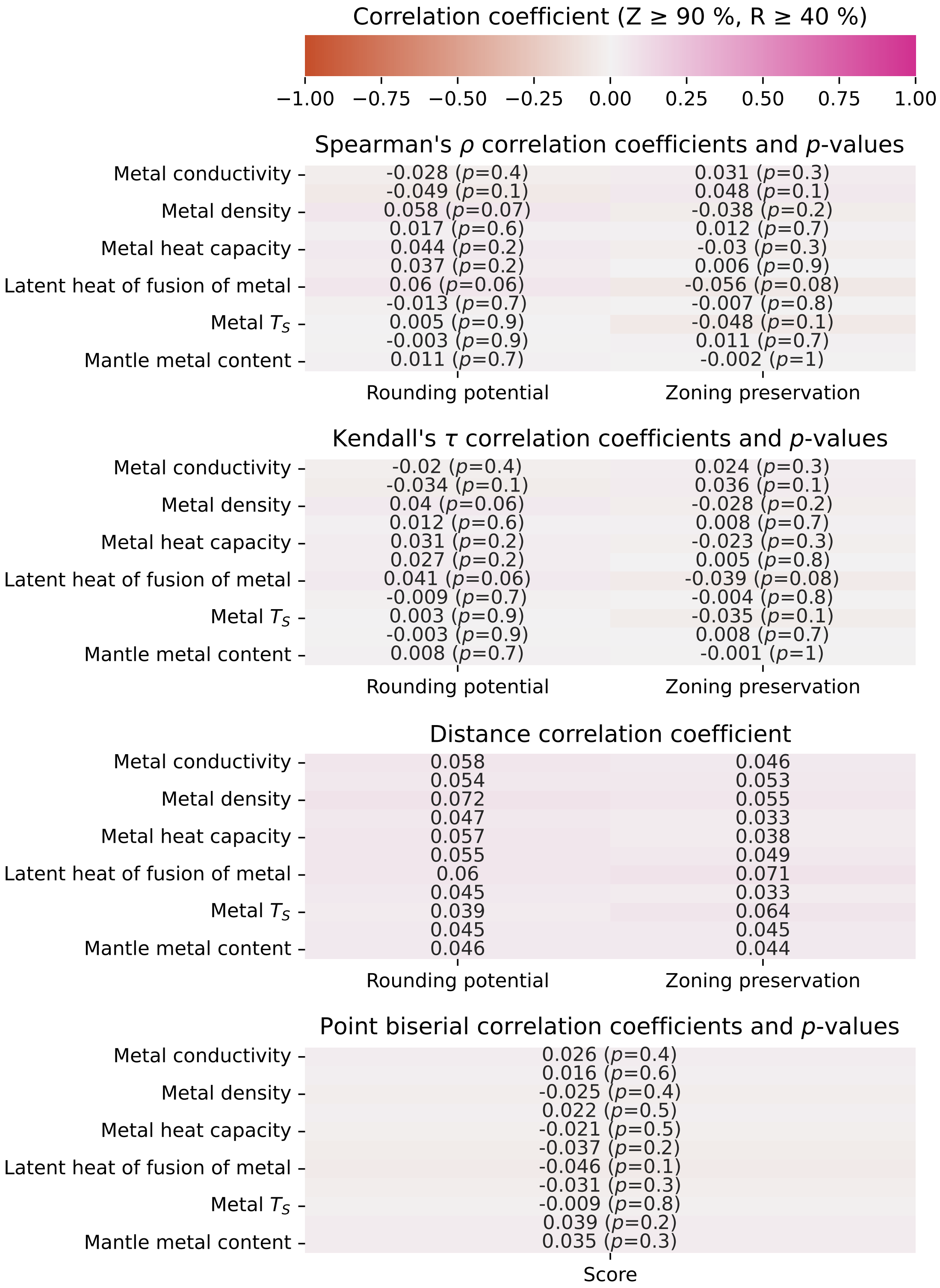

Figure S14: Monotonic and non-monotonic estimations of correlation with p value where relevant, for a suite of initial conditions (specifically relating to material properties) and resulting volume % that match the rounding and zoning preservation criteria, as well as the overall score (where score was reduced to a binary pass/fail, with scores of 0 and 1 grouped into the fail category).

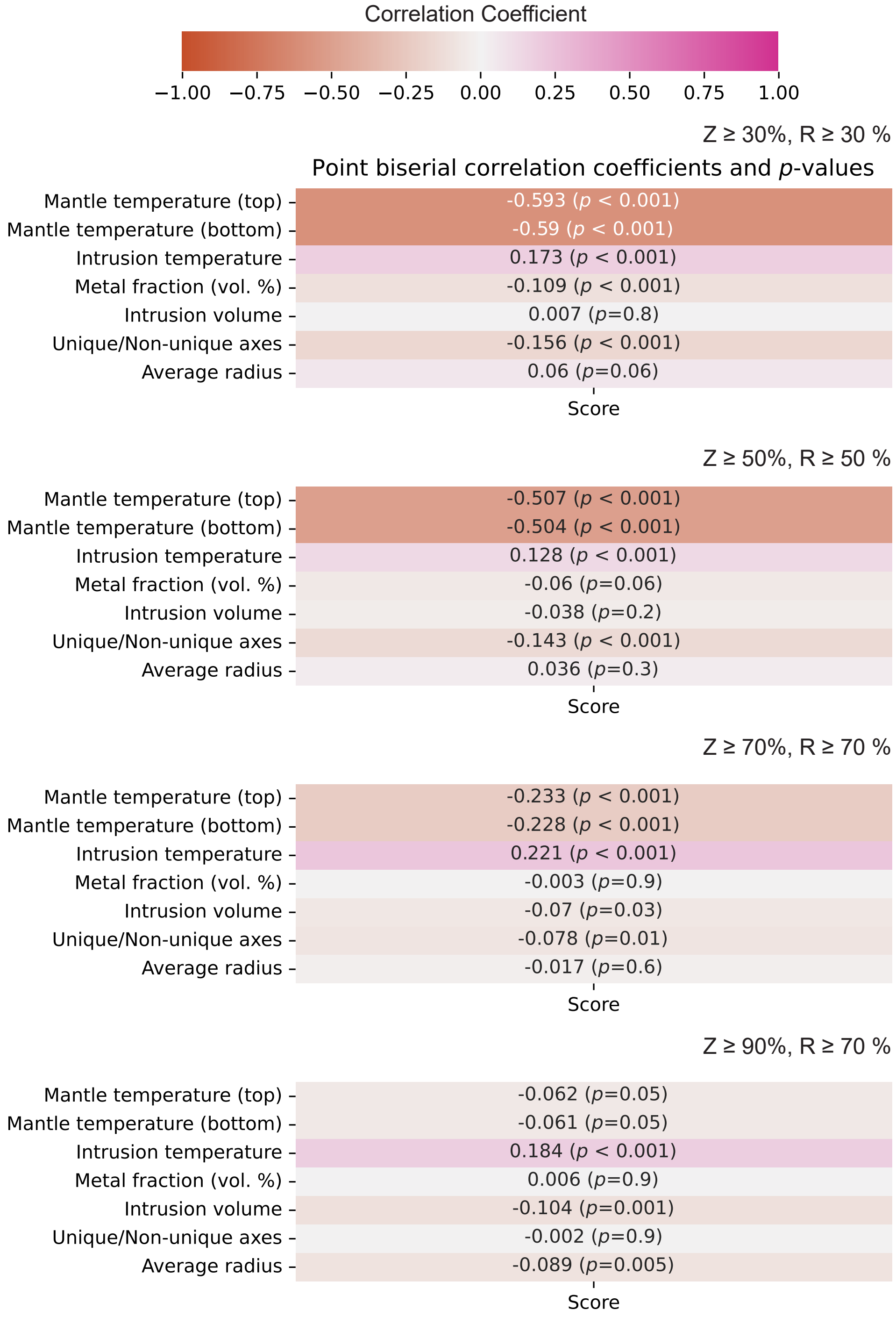

Z ≥ 30%, R ≥ 30 %

Point biserial correlation coefficients and *p*-values

	Score
Mantle temperature (top)	-0.593 (p < 0.001)
Mantle temperature (bottom)	-0.59 (p < 0.001)
Intrusion temperature	0.173 (p < 0.001)
Metal fraction (vol. %)	-0.109 (p < 0.001)
Intrusion volume	0.007 (p=0.8)
Unique/Non-unique axes	-0.156 (p < 0.001)
Average radius	0.06 (p=0.06)

Z ≥ 50%, R ≥ 50 %

	Score
Mantle temperature (top)	-0.507 (p < 0.001)
Mantle temperature (bottom)	-0.504 (p < 0.001)
Intrusion temperature	0.128 (p < 0.001)
Metal fraction (vol. %)	-0.06 (p=0.06)
Intrusion volume	-0.038 (p=0.2)
Unique/Non-unique axes	-0.143 (p < 0.001)
Average radius	0.036 (p=0.3)

Z ≥ 70%, R ≥ 70 %

	Score
Mantle temperature (top)	-0.233 (p < 0.001)
Mantle temperature (bottom)	-0.228 (p < 0.001)
Intrusion temperature	0.221 (p < 0.001)
Metal fraction (vol. %)	-0.003 (p=0.9)
Intrusion volume	-0.07 (p=0.03)
Unique/Non-unique axes	-0.078 (p=0.01)
Average radius	-0.017 (p=0.6)

Z ≥ 90%, R ≥ 70 %

	Score
Mantle temperature (top)	-0.062 (p=0.05)
Mantle temperature (bottom)	-0.061 (p=0.05)
Intrusion temperature	0.184 (p < 0.001)
Metal fraction (vol. %)	0.006 (p=0.9)
Intrusion volume	-0.104 (p=0.001)
Unique/Non-unique axes	-0.002 (p=0.9)
Average radius	-0.089 (p=0.005)

Figure S15: Point biserial estimations of correlation with p values, for a suite of initial conditions and the resulting overall score (where score was reduced to a binary pass/fail, with scores of 0 and 1 grouped into the fail category).

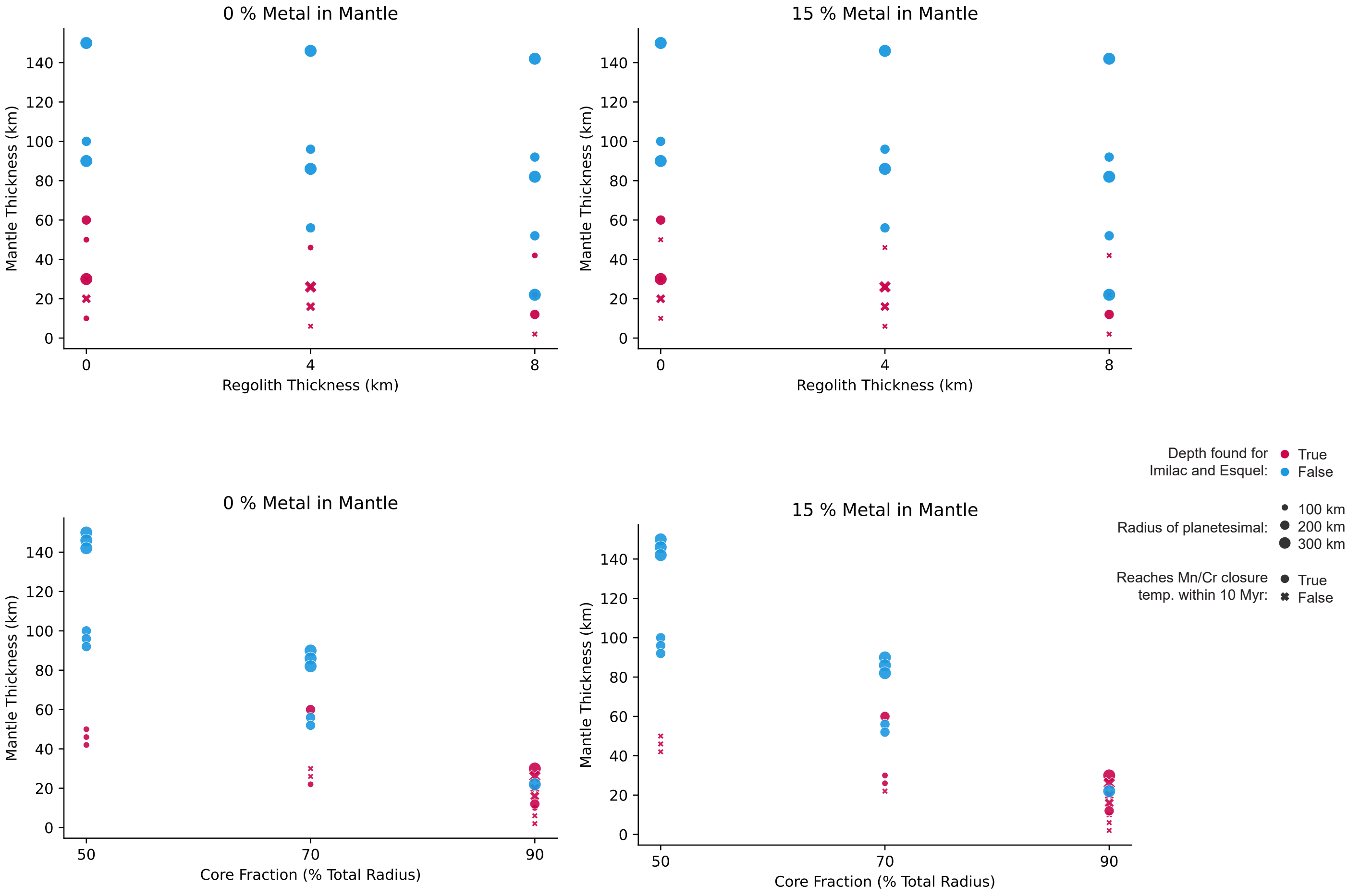

Figure S16: Meteorite depth calculation results for varied planetesimal geometries and mantle metal content.

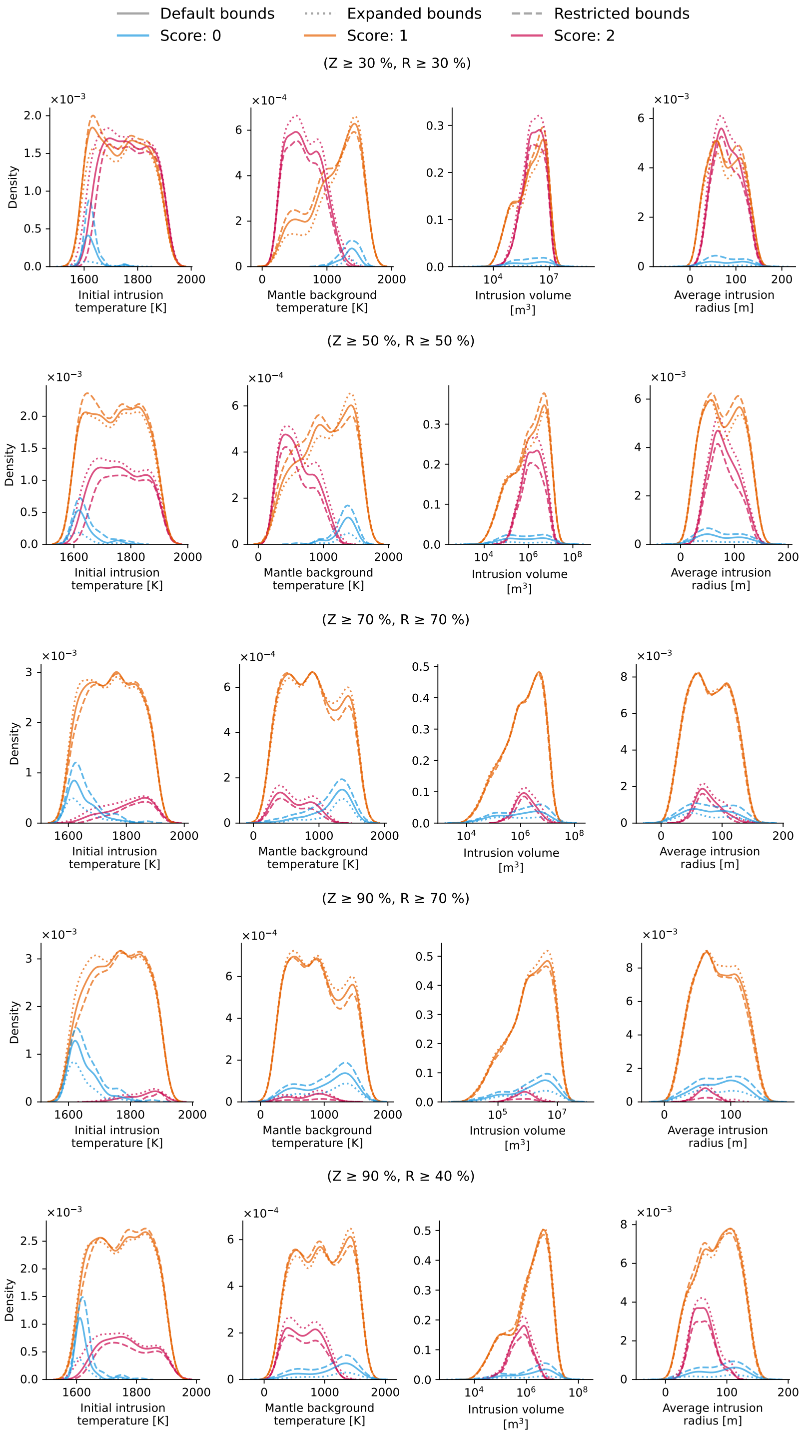

Figure S17: Kernel density estimates for model score vs. initial intrusion temperature, background mantle temperature, intrusion volume (log scale) and average intrusion radius, showing change with "restricted" and "expanded" bounds (±10 %), for different constraint filters. "Restricting" the bounds makes it more difficult for a model to pass the requirements, by increasing the rounding temperature cut-off by +10 %, and decreasing the zoning temperature cut-off by −10 %. "Expanding" the bounds is the opposite; by increasing the zoning temperature cut-off by +10 %, and decreasing the rounding temperature cut-off by −10 %, resulting in more models with a score of 2.

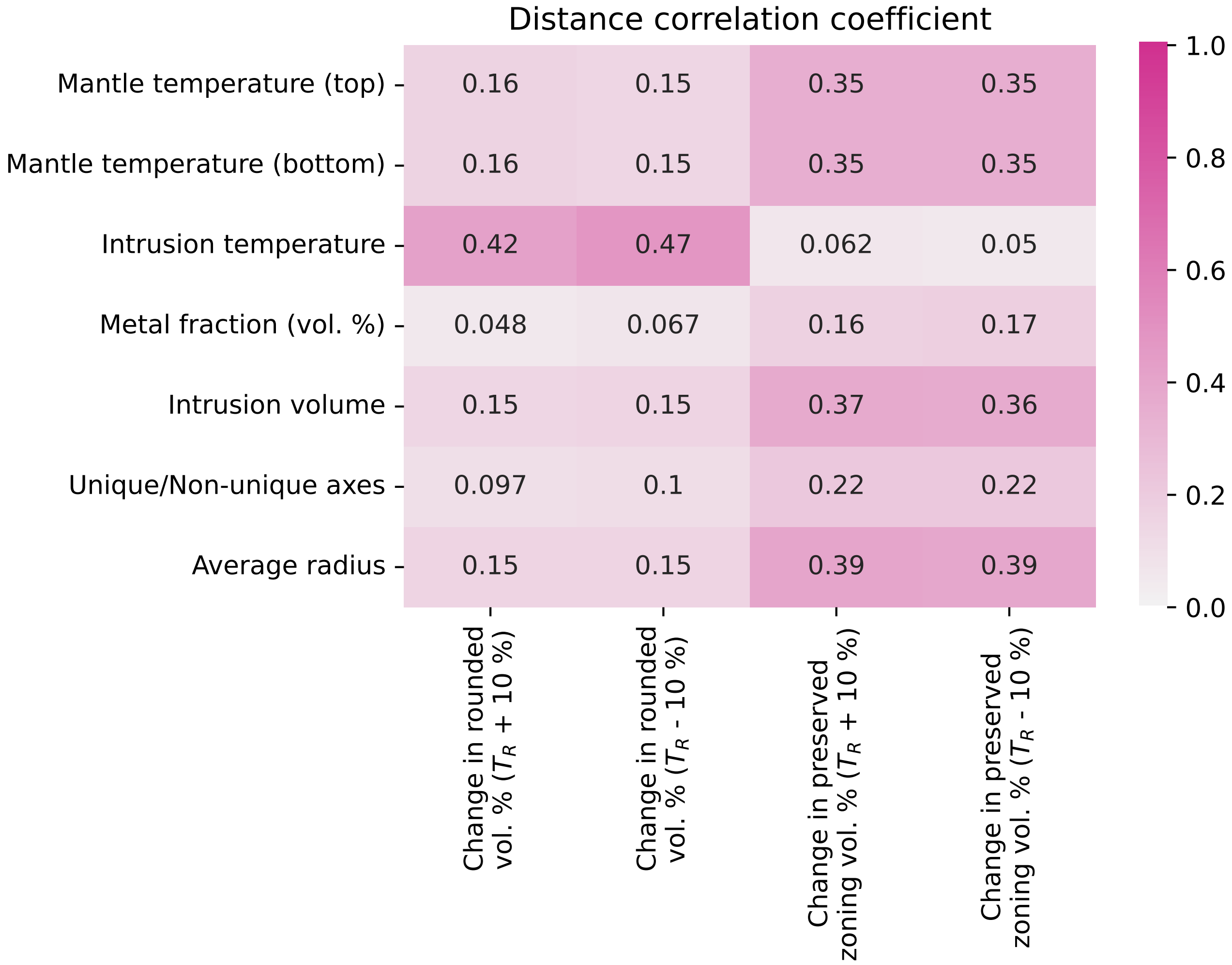

	Change in rounded vol. % (T_R + 10 %)	Change in rounded vol. % (T_R - 10 %)	Change in preserved zoning vol. % (T_R + 10 %)	Change in preserved zoning vol. % (T_R - 10 %)
Mantle temperature (top)	0.16	0.15	0.35	0.35
Mantle temperature (bottom)	0.16	0.15	0.35	0.35
Intrusion temperature	0.42	0.47	0.062	0.05
Metal fraction (vol. %)	0.048	0.067	0.16	0.17
Intrusion volume	0.15	0.15	0.37	0.36
Unique/Non-unique axes	0.097	0.1	0.22	0.22
Average radius	0.15	0.15	0.39	0.39

Figure S18: Non-monotonic distance correlation between change in volume % rounded and volume % zoning preserved when the temperature filters are changed by ±10 % of the original temperature, and parameters such as mantle temperature, intrusion temperature, and intrusion geometry.

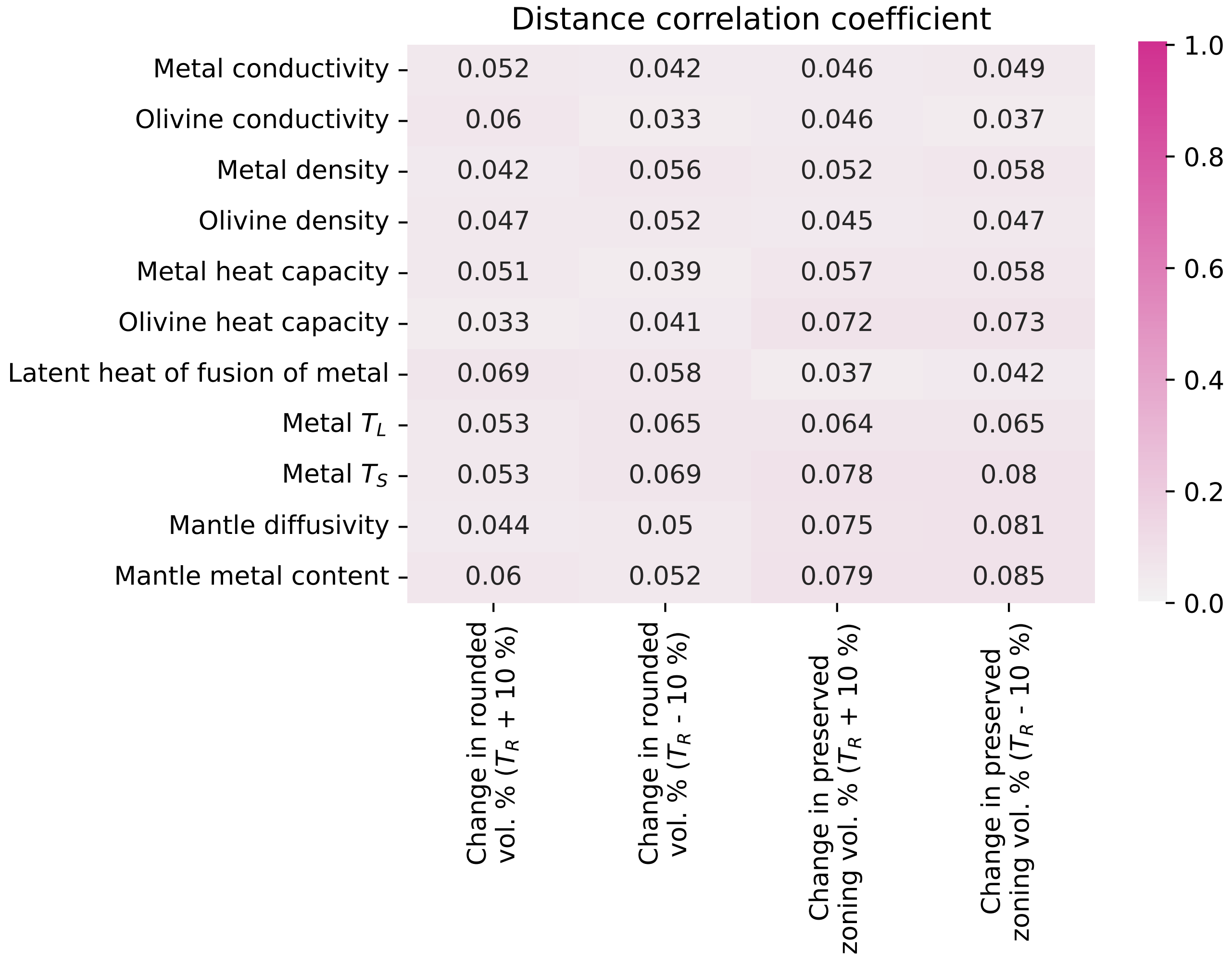

	Change in rounded vol. % (T_R + 10 %)	Change in rounded vol. % (T_R - 10 %)	Change in preserved zoning vol. % (T_R + 10 %)	Change in preserved zoning vol. % (T_R - 10 %)
Metal conductivity	0.052	0.042	0.046	0.049
Olivine conductivity	0.06	0.033	0.046	0.037
Metal density	0.042	0.056	0.052	0.058
Olivine density	0.047	0.052	0.045	0.047
Metal heat capacity	0.051	0.039	0.057	0.058
Olivine heat capacity	0.033	0.041	0.072	0.073
Latent heat of fusion of metal	0.069	0.058	0.037	0.042
Metal T_L	0.053	0.065	0.064	0.065
Metal T_S	0.053	0.069	0.078	0.08
Mantle diffusivity	0.044	0.05	0.075	0.081
Mantle metal content	0.06	0.052	0.079	0.085

Figure S19: Non-monotonic distance correlation between change in volume % rounded and volume % zoning preserved when the temperature filters are changed by ±10 % of the original temperature, and parameters relating to the material properties of the intrusion region.

Table S1: Summary of model runs for sensitivity testing; results shown in Figures S10, S11. $L_{x,y,z} = 400$ m, $\Delta x, y, z = 2$ m, $r_{x,y,z} = 80$ m, material properties of metal and olivine set equal to example case in the main text. Values listed below were set to the mean value (in **bold**) unless they were being varied.

	Step:	**-1**	**-0.5**	**0**	**0.5**	**1**
Parameter varied	**Unit**	Minimum		Mean		Maximum
Liquidus Temperature	K	1570	1630.25	**1690.5**	1750.75	1811
Solidus Temperature	K	1260	1395	**1530**	1665	1800
Liquidus and Solidus Temperatures	K					
Initial intrusion temperature	K	1600	1700	**1800**	1900	2000
Background mantle temperature	K	250	637.5	**1025**	1412.5	1800
Metal fraction	Volume fraction	0.1	0.2	**0.3**	0.4	0.5
Latent heat	J/kg	133000	163750	**194500**	225250	256000

Table S2: Summary of results, with absolute numbers of models receiving each score, and percentage of the model set with a score of 2 (passing both constraints).

	Total number	Score = 0	Score = 1	Score = 2	% Score = 2
(Z $\geq$ 90 %, R $\geq$ 40 %)					
Full dataset	2200	145	849	276	12.55
Planetesimal input	600	44	497	59	9.83
r = 250 km	299	24	250	25	8.36
r = 300 km	301	20	247	34	11.30
Randomly varied material prop.	1000	55	759	186	18.60
Increase filters by +10 %	1000	82	741	177	8.20
Decrease filters by -10 %	1000	26	776	198	2.60
Expand filters by 10 %	1000	24	752	224	2.40
Restrict filters by 10 %	1000	89	755	156	8.90

Table S3: Summary of results, with absolute numbers of models receiving each score, and percentage of the model set with a score of 2 (passing both constraints).

(Z ≥ 30 %, R ≥ 30 %)	Total number	Score = 0	Score = 1	Score = 2	% Score = 2
Full dataset	2200	70	562	506	23.00
Planetesimal input	600	23	403	174	29.00
r = 250 km	299	18	204	77	25.75
r = 300 km	301	5	199	97	32.23
Randomly varied material prop.	1000	24	516	460	46.00
Increase filters by +10 %	1000	39	523	438	3.90
Decrease filters by -10 %	1000	9	500	491	0.90
Expand filters by 10 %	1000	8	475	517	0.80
Restrict filters by 10 %	1000	44	540	416	4.40

(Z ≥ 50 %, R ≥ 50 %)	Total number	Score = 0	Score = 1	Score = 2	% Score = 2
Full dataset	2200	100	696	384	17.45
Planetesimal input	600	30	470	100	16.67
r = 250 km	299	20	239	40	13.38
r = 300 km	301	10	231	60	19.93
Randomly varied material prop.	1000	40	636	324	32.40
Increase filters by +10 %	1000	55	648	297	5.50
Decrease filters by -10 %	1000	20	642	338	2.00
Expand filters by 10 %	1000	15	616	369	1.50
Restrict filters by 10 %	1000	63	668	269	6.30

(Z ≥ 70 %, R ≥ 70 %)	Total number	Score = 0	Score = 1	Score = 2	% Score = 2
Full dataset	2200	234	983	245	11.14
Planetesimal input	600	83	492	25	4.17
r = 250 km	299	44	245	10	3.34
r = 300 km	301	39	247	15	4.98
Randomly varied material prop.	1000	80	829	91	9.10
Increase filters by +10 %	1000	105	812	83	10.50
Decrease filters by -10 %	1000	59	845	96	5.90
Expand filters by 10 %	1000	49	834	117	4.90
Restrict filters by 10 %	1000	122	809	69	12.20

(Z ≥ 90 %, R ≥ 70 %)	Total number	Score = 0	Score = 1	Score = 2	% Score = 2
Full dataset	2200	320	1059	230	10.45
Planetesimal input	600	103	489	8	1.33
r = 250 km	299	54	241	4	1.34
r = 300 km	301	49	248	4	1.33
Randomly varied material prop.	1000	117	856	27	2.70
Increase filters by +10 %	1000	144	835	21	14.40
Decrease filters by -10 %	1000	85	891	24	8.50
Expand filters by 10 %	1000	71	891	38	7.10
Restrict filters by 10 %	1000	162	827	11	16.20

Table S4: Rapidly cooling planetesimals with estimated pallasite meteorite residence depths (if a fit could be found). Temperature 10 Myr is calculated at Imilac's residence depth, and then additionally for residence depths of pallasites recording cooling of 1 K/Myr and 10 K/Myr (if depths could be calculated). Models that have cooled below the Mn-Cr closure temperature by 10 Myr are shown in bold (see discussion in main text).

Radius (km)	Core Size (% of radius)	Regolith Thickness (km)	Initial Mantle Temp. (K)	Im. Depth (km)	Temp. at Im. depth, 10 Myr (K)	Temp. at 10 K/Myr depth, 10 Myr (K)	Temp. at 1 K/Myr. depth, 10 Myr (K)	Im. match	Mn/Cr closure match	Trapped metal in mantle
100.0	0.5	0	1700	38.0	1505.597011	1462.120375	NaN	y	n	0 %
100.0	0.9	0	1700	7.0	928.126883	NaN	928.126883	y	y	0 %
100.0	0.5	4	1700	38.0	1577.917771	1545.787536	NaN	y	n	0 %
100.0	0.7	8	1700	21.0	1531.818939	1509.984571	NaN	y	n	0 %
200.0	0.7	0	1700	34.0	1473.009147	1313.546381	1604.121965	y	n	0 %
200.0	0.9	4	1700	13.0	1420.470434	1288.092526	NaN	y	y	0 %
300.0	0.9	0	1700	NaN	NaN	NaN	1157.135272	n	y	0 %
100.0	0.7	0	1700	NaN	NaN	1096.863412	NaN	n	y	15 %
100.0	0.7	4	1700	NaN	NaN	1185.471206	NaN	n	y	15 %
200.0	0.7	0	1700	34.0	1473.009147	1313.546381	1604.121965	y	n	15 %
200.0	0.9	4	1700	13.0	1420.470434	1288.092526	NaN	y	y	15 %
300.0	0.9	0	1700	NaN	NaN	NaN	1157.135272	n	y	15 %
100.0	0.5	0	1800	38.0	1599.557230	1553.719945	NaN	y	n	0 %
100.0	0.9	0	1800	7.0	949.810277	NaN	949.810277	y	y	0 %
100.0	0.5	4	1800	38.0	1675.739597	1642.279220	NaN	y	n	0 %
100.0	0.7	8	1800	21.0	1623.426411	1600.243709	NaN	y	n	0 %
200.0	0.7	0	1800	33.0	1540.124698	1359.825911	1702.295171	y	n	0 %
200.0	0.9	4	1800	13.0	1502.676967	NaN	NaN	y	n	0 %
300.0	0.9	0	1800	NaN	NaN	888.005961	1219.595710	n	y	0 %
100.0	0.7	0	1800	NaN	NaN	1157.174248	NaN	n	y	15 %
100.0	0.7	4	1800	NaN	NaN	1254.705229	NaN	n	y	15 %
200.0	0.7	0	1800	33.0	1540.124698	1359.825911	1702.295171	y	n	15 %
200.0	0.9	4	1800	13.0	1502.676967	NaN	NaN	y	y	15 %
300.0	0.9	0	1800	NaN	NaN	888.005961	1219.595710	n	y	15 %

Table S5: Temperatures at depths within rapidly cooling planetesimals. Temperatures at 7 Myr and 10 Myr are calculated at Imilac's residence depth, and then additionally for residence depths of pallasites recording cooling of 1 K/Myr and 10 K/Myr (if depths could be calculated). Models that have cooled below the Mn-Cr closure temperature by 10 Myr are shown in bold (see discussion in main text). In order to enable early rounding of large pallasite olivine in a region of the parent body, we require $T_m \geq 1673$ K until/at 7 Ma (Saiki et al., 2003)

Radius (km)	Core Size (% of radius)	Regolith Thickness (km)	Initial Mantle Temp. (K)	Im. Depth (km)	Temp. at Im. depth, 10 Myr (K)	Temp. at 10 K/Myr depth, 10 Myr (K)	Temp. at 1 K/Myr. depth, 10 Myr (K)	Trapped metal in mantle	Temp. at Im. depth, 7 Myr (K)	Temp. at 10 K/Myr depth, 7 Myr (K)	Temp. at 1 K/Myr. depth, 7 Myr (K)
100.0	0.5	0	1700	38.0	1505.6	1462.1	NaN	0 %	1620.6	1594.6	NaN
100.0	0.9	0	1700	7.0	928.1	NaN	928.1	0 %	1006.1	NaN	1006.1
100.0	0.5	4	1700	38.0	1577.9	1545.8	NaN	0 %	1664.5	1650.6	NaN
100.0	0.7	8	1700	21.0	1531.8	1510.0	NaN	0 %	1628.6	1616.6	NaN
200.0	0.7	0	1700	34.0	1473.0	1313.5	1604.1	0 %	1592.1	1468.9	1668.2
200.0	0.9	4	1700	13.0	1420.5	1288.1	NaN	0 %	1532.9	1437.8	NaN
300.0	0.9	0	1700	NaN	NaN	NaN	1157.1	0 %	NaN	NaN	1250.4
100.0	0.7	0	1700	NaN	NaN	1218.9	NaN	15 %	NaN	1218.9	NaN
100.0	0.7	4	1700	NaN	NaN	1361.1	NaN	15 %	NaN	1361.1	NaN
200.0	0.7	0	1700	34.0	1592.1	1468.9	1668.2	15 %	1592.1	1468.9	1668.2
200.0	0.9	4	1700	13.0	1532.9	1437.8	NaN	15 %	1532.9	1437.8	NaN
300.0	0.9	0	1700	NaN	NaN	NaN	1250.4	15 %	NaN	NaN	1250.4
100.0	0.5	0	1800	38.0	1599.6	1553.7	NaN	0 %	1620.6	1594.6	NaN
100.0	0.9	0	1800	7.0	949.8	NaN	949.8	0 %	1006.1	NaN	1006.1
100.0	0.5	4	1800	38.0	1675.7	1642.3	NaN	0 %	1664.5	1650.6	NaN
100.0	0.7	8	1800	21.0	1623.4	1600.2	NaN	0 %	1628.6	1616.6	NaN
200.0	0.7	0	1800	33.0	1540.1	1359.8	1702.3	0 %	1592.1	1468.9	1668.2
200.0	0.9	4	1800	13.0	1502.7	NaN	NaN	0 %	1532.9	1437.8	NaN
300.0	0.9	0	1800	NaN	NaN	888.0	1219.6	0 %	NaN	NaN	1250.4
100.0	0.7	0	1800	NaN	NaN	1157.2	NaN	15 %	NaN	1218.9	NaN
100.0	0.7	4	1800	NaN	NaN	1254.7	NaN	15 %	NaN	1361.1	NaN
200.0	0.7	0	1800	33.0	1540.1	1359.8	1702.3	15 %	1592.1	1468.9	1668.2
200.0	0.9	4	1800	13.0	1502.7	NaN	NaN	15 %	1532.9	1437.8	NaN
300.0	0.9	0	1800	NaN	NaN	888.0	1219.6	15 %	NaN	NaN	1250.4

Table S6: Parameters and results for a selection of models with initial background mantle temperatures ≥ 1250 K.

Background mantle temp. (top, K)	Background mantle temp. (bottom, K)	Initial intrusion temp. (K)	r_x (m)	r_y (m)	r_z (m)	$\overline{r}$ (m)	Metal fraction (intrusion)	Intrusion volume (m^3)	Vol. % rounded	Vol. % zoned
1325	1325	1700	20	30	60	36.7	0.35	149,392	53	1
1300	1300	1700	20	30	60	36.7	0.35	149,392	51	16
1275	1275	1700	20	30	60	36.7	0.35	149,392	50	54
1250	1300	1700	20	30	60	36.7	0.35	149,392	50	54
1250	1325	1700	20	30	60	36.7	0.35	149,392	51	31
1325	1325	1800	20	30	60	36.7	0.35	149,392	80	0
1300	1300	1800	20	30	60	36.7	0.35	149,392	77	4
1275	1275	1800	20	30	60	36.7	0.35	149,392	75	19
1250	1300	1800	20	30	60	36.7	0.35	149,392	75	19
1250	1325	1800	20	30	60	36.7	0.35	149,392	76	10
1325	1325	1800	20	20	90	43.3	0.35	149,608	76	4
1300	1300	1800	20	20	90	43.3	0.35	149,608	73	17
1275	1275	1800	20	20	90	43.3	0.35	149,608	71	41
1250	1300	1800	20	20	90	43.3	0.35	149,608	71	41
1250	1325	1800	20	20	90	43.3	0.35	149,608	72	27

Table S7: Parameters and results for a selection of models with initial background mantle temperatures ≥ 1250 K.

Background mantle temp. (top, K)	Background mantle temp. (bottom, K)	Initial intrusion temp. (K)	r_x (m)	r_y (m)	r_z (m)	$\overline{r}$ (m)	Metal fraction (intrusion)	Intrusion volume (m^3)	Vol. % rounded	Vol. % zoned
1325	1325	1700	80	30	60	56.7	0.35	601,336	72	0
1300	1300	1700	80	30	60	56.7	0.35	601,336	70	0
1275	1275	1700	80	30	60	56.7	0.35	601,336	69	0
1250	1300	1700	80	30	60	56.7	0.35	601,336	69	0
1250	1325	1700	80	30	60	56.7	0.35	601,336	70	0
1325	1325	1800	80	30	60	56.7	0.35	601,336	90	0
1300	1300	1800	80	30	60	56.7	0.35	601,336	88	0
1275	1275	1800	80	30	60	56.7	0.35	601,336	87	0
1250	1300	1800	80	30	60	56.7	0.35	601,336	87	0
1250	1325	1800	80	30	60	56.7	0.35	601,336	87	0
1325	1325	1800	80	20	90	63.3	0.35	600,848	88	0
1300	1300	1800	80	20	90	63.3	0.35	600,848	85	0
1275	1275	1800	80	20	90	63.3	0.35	600,848	83	2
1250	1300	1800	80	20	90	63.3	0.35	600,848	83	2
1250	1325	1800	80	20	90	63.3	0.35	600,848	84	1

References

J. S. Boesenberg, J. S. Delaney, and R. H. Hewins. A petrological and chemical reexamination of main group pallasite formation. *Geochimica et Cosmochimica Acta*, 89:134–158, July 2012. doi: 10.1016/j.gca.2012.04.037. URL `https://doi.org/10.1016/j.gca.2012.04.037`.

H. S. Carslaw and J. C. Jaeger. *Conduction of heat in solids.* Clarendon Press ; Oxford University Press, Oxford : New York, 2nd edition, 1959.

W. Cen, R. Hoppe, and N. Gu. Fast and accurate determination of 3D temperature distribution using fraction-step semi-implicit method. *AIP Advances*, 6(9):095305, 2016. doi: 10.1063/1.4962665.

J. Crank and P. Nicolson. A practical method for numerical evaluation of solutions of partial differential equations of the heat-conduction type. *Mathematical Proceedings of the Cambridge Philosophical Society*, 43(1):50–67, 1947. doi: 10.1017/s0305004100023197.

H. P. Langtangen and S. Linge. *Finite Difference Computing with PDEs.* Springer International Publishing, 2017. doi: 10.1007/978-3-319-55456-3. URL `https://doi.org/10.1007/978-3-319-55456-3`.

D. Mottaghy and V. Rath. Latent heat effects in subsurface heat transport modelling and their impact on palaeotemperature reconstructions. *Geophysical Journal International*, 164(1):236–245, 2006. doi: 10.1111/j.1365-246x.2005.02843.x.

M. Özısık. *Heat conduction.* Wiley, New York, 1993.

R. Roy, A. Beck, and Y. Touloukian. Thermo-Physical Properties of Rocks. *McGraw-Hill CINDAS Data Series on Material Properties*, 11:409–502, 1981.

S. Sahijpal. Thermal evolution of non-spherical asteroids in the early solar system. *Icarus*, page 114439, 2021. doi: 10.1016/j.icarus.2021.114439.

K. Saiki, D. Laporte, D. Vielzeuf, S. Nakashima, and P. Boivin. Morphological analysis of olivine grains annealed in an iron-nickel matrix: Experimental constraints on the origin of pallasites and on the thermal history of their parent bodies. *Meteoritics & Planetary Science*, 38(3):427–444, 2003.

I. Sarbu and C. Sebarchievici. Thermal Energy Storage. In *Solar Heating and Cooling Systems: Fundamentals, Experiments and Applications*, pages 99–138. Elsevier, 2017. doi: 10.1016/b978-0-12-811662-3.00004-9.

J. T. Wasson and B.-G. Choi. Main-group pallasites. *Geochimica et Cosmochimica Acta*, 67(16):3079–3096, 2003. doi: 10.1016/s0016-7037(03)00306-5.

N. N. Yanenko. *The Method of Fractional Steps.* Springer Berlin Heidelberg, 1971. doi: 10.1007/978-3-642-65108-3.

M. Zeneli, A. Nikolopoulos, S. Karellas, and N. Nikolopoulos. Numerical methods for solid-liquid phase-change problems. In *Ultra-High Temperature Thermal Energy Storage, Transfer and Conversion*, pages 165–199. Elsevier, 2021. doi: 10.1016/b978-0-12-819955-8.00007-7.